

From Generative Modeling to Clinical Classification: A GPT-Based Architecture for EHR Notes

Fariba Afrin Irany

Abstract

The increasing availability of unstructured clinical narratives in electronic health records (EHRs) has created new opportunities for automated disease characterization, cohort identification, and clinical decision support. However, effectively modeling long, domain-specific clinical text remains challenging due to limited labeled data, substantial class imbalance, and the high computational cost associated with adapting large pretrained language models to downstream tasks.

In this study, a GPT-based architecture for clinical text classification is presented, which adapts a pretrained decoder-only Transformer to downstream clinical tasks using a selective fine-tuning strategy. Instead of updating all model parameters, the majority of the pretrained GPT-2 backbone is frozen, and training is restricted to the final Transformer block, the final layer normalization, and a lightweight classification head. This design significantly reduces the number of trainable parameters while preserving the representational capacity required for modeling complex clinical language.

This study evaluates the proposed approach on radiology reports from the MIMIC-IV-Note dataset using uncertainty-aware CheXpert-style labels derived directly from report text. Experiments are conducted across multiple problem formulations, including multi-label classification of radiographic findings, binary per-label classification under different uncertainty assumptions, and aggregate disease outcome prediction. Across varying sample sizes, the model demonstrates stable convergence behavior and strong classification performance, particularly in multi-class settings where non-mention and negated findings are prevalent.

Overall, the results suggest that selective fine-tuning of pretrained generative language models offers an efficient and effective pathway for clinical text classification, enabling scalable adaptation to real-world EHR data while substantially reducing computational complexity.

Keywords: clinical natural language processing; large language models; GPT; radiology report classification; uncertainty-aware labeling; MIMIC-IV

Introduction

The widespread adoption of electronic health record (EHR) systems has led to an unprecedented growth in the volume of unstructured clinical text. Clinical narratives such as progress notes, discharge summaries, operative reports, and radiology interpretations capture detailed information about patient history, physician reasoning, and care trajectories that is often unavailable in structured fields. Extracting meaningful

information from these free-text documents is essential for a wide range of downstream applications, including disease phenotyping, cohort discovery, outcome prediction, quality assessment, and clinical decision support. However, the unstructured and highly specialized nature of clinical language poses substantial challenges for automated analysis.

Traditional natural language processing approaches in the clinical domain have relied heavily on rule-based systems, domain-specific lexicons, or manually engineered features. While these methods can be effective for narrowly defined tasks, they are often brittle, difficult to scale, and unable to capture long-range dependencies or nuanced contextual meaning. Statistical machine learning methods improved flexibility but still required substantial feature engineering and struggled with the variability and complexity of clinical narratives. These limitations have motivated the adoption of representation learning approaches that can automatically learn contextual features directly from raw text.

Transformer-based language models have emerged as a dominant paradigm for representation learning in natural language processing. By relying on self-attention mechanisms, Transformers are able to model long-range dependencies and contextual interactions between tokens more effectively than recurrent or convolutional architectures. Large language models pretrained on massive text corpora using self-supervised objectives have demonstrated remarkable generalization capabilities, enabling transfer learning across a wide range of downstream tasks. Generative pretrained models, such as GPT-2, learn rich contextual representations by predicting tokens autoregressively, allowing them to capture syntactic structure, semantic relationships, and discourse-level patterns in text.

Despite these advances, directly applying large pretrained language models to clinical text introduces several practical and methodological challenges. Clinical datasets are typically orders of magnitude smaller than the corpora used for pre-training, increasing the risk of overfitting during downstream training. Moreover, the computational cost of fine-tuning all parameters of a large language model can be prohibitive, particularly in academic or clinical environments with limited computational resources. Full fine-tuning also increases memory usage during training due to the need to store gradients and optimizer states for all parameters, further constraining scalability.

An additional challenge arises from the domain mismatch

between general-language pretraining data and clinical text. While pretrained models capture broad linguistic knowledge, clinical narratives exhibit unique characteristics, including specialized terminology, abbreviations, telegraphic writing styles, and institution-specific conventions. Effective adaptation therefore requires balancing domain-specific learning with preservation of general-language representations. Updating too many parameters risks catastrophic forgetting of pretrained knowledge, while updating too few parameters may limit the model’s ability to adapt.

To address these challenges, this work explores a selective fine-tuning strategy for adapting GPT-2 to unstructured clinical text classification tasks. Instead of updating the entire model, the majority of pretrained parameters are frozen, and optimization is restricted to a carefully chosen subset of layers. Specifically, only the final Transformer block, the final layer normalization, and a lightweight task-specific classification head are updated during fine-tuning. This design leverages the hierarchical nature of Transformer representations, where lower layers tend to encode general linguistic features and higher layers capture more abstract, task-relevant information.

A key contribution of this work is a detailed and transparent analysis of model parameterization and computational complexity under this selective fine-tuning regime. While selective fine-tuning is often motivated intuitively, its concrete impact on parameter count and training-time complexity is rarely made explicit. In this paper, the number of frozen and trainable parameters in the GPT-2 (small) architecture is quantified, demonstrating that more than ninety-four percent of the model parameters remain fixed during training. A further analysis examines how restricting backpropagation to a single Transformer block substantially reduces training-time complexity and memory requirements while still enabling effective task adaptation.

This work is intentionally written to be accessible to readers who may be new to large language models and Transformer architectures. Rather than assuming familiarity with internal model mechanics, step-by-step explanations are provided to clarify how parameters are distributed across model components, why specific terms arise in the complexity analysis, and how architectural design choices influence computational efficiency. By making these details explicit, selective fine-tuning strategies are demystified, and practical guidance is provided for researchers seeking to apply large language models in data-limited or resource-constrained settings.

Overall, this study demonstrates that efficient adaptation of generative pretrained language models to clinical text is possible without full-model fine-tuning. By combining selective parameter optimization with a clear understanding of architectural complexity, the proposed approach offers a practical and computationally efficient pathway for deploying large language models in clinical natural language processing applications.

This work makes the following contributions:

- A parameter-efficient selective fine-tuning strategy for

GPT-based clinical text classification that updates only a small subset of model parameters.

- A systematic analysis of training dynamics and computational trade-offs associated with selective fine-tuning.
- An empirical evaluation on large-scale MIMIC-IV radiology reports demonstrating competitive performance under constrained computational resources.

Literature Review

This literature review situates the proposed selective fine-tuning framework within four intersecting research areas: (i) Transformer-based language models and large-scale pretraining, (ii) transfer learning and domain adaptation for NLP, (iii) parameter-efficient fine-tuning and computationally efficient adaptation, and (iv) clinical NLP and modeling unstructured EHR narratives.

Transformer Architectures and Large-Scale Language Model Pretraining

The Transformer architecture introduced self-attention as the core mechanism for sequence modeling, enabling efficient parallel computation and strong performance on machine translation and beyond Vaswani et al., 2017. Subsequent work clarified optimization and architectural details relevant to deep Transformer training, including the role of normalization and residual design Ba, Kiros, and Hinton, 2016; “On layer normalization in the Transformer architecture,” 2020. The broad adoption of Transformers led to the development of large pretrained language models trained with self-supervised objectives, which learn reusable linguistic representations.

Early milestones in language model pretraining include ELMo Peters et al., 2018 and ULMFiT Howard and Ruder, 2018, which established that pretrained representations can dramatically improve downstream task performance. GPT-style models popularized decoder-only autoregressive pretraining at scale Brown et al., 2020; Radford et al., 2018, 2019, while BERT introduced deep bidirectional masked language modeling and demonstrated strong transfer to many downstream tasks Devlin et al., 2019. Several influential architectural or training enhancements further improved scale and stability, including RoBERTa Y. Liu et al., 2019, ALBERTa Lan et al., 2020, XLNet Yang et al., 2019, T5 Raffel et al., 2020, and ELECTRA Clark et al., 2020. Improvements in Transformer efficiency and long-context handling have been explored through sparse or reformulated attention mechanisms such as Transformer-XL Dai et al., 2019, Longformer Beltagy et al., 2020, BigBird Zaheer et al., 2020, Reformer Kitaev et al., 2020, Linformer Wang et al., 2020, and Performer Choromanski et al., 2021. Collectively, these works provide the foundation for applying pretrained Transformer representations to specialized domains, including clinical narratives, where long-range dependencies and context sensitivity are essential.

Transfer Learning, Domain Adaptation, and Continued Pretraining

A central motivation for pretrained language models is their ability to transfer linguistic knowledge to data-scarce tasks. General transfer learning principles and empirical studies show that features learned in large models can be reused across tasks, although transferability depends on layer depth and domain similarity Peters et al., 2019; Yosinski et al., 2014a. In NLP, domain adaptation can be achieved through continued pretraining on domain-specific corpora prior to supervised fine-tuning. Gururangan et al. demonstrated that continued pretraining (domain-adaptive pretraining and task-adaptive pretraining) provides systematic gains in specialized domains Gururangan et al., 2020. Similar observations appear in biomedical and clinical language modeling, where domain-specific corpora and terminologies differ substantially from general web text.

Within biomedical NLP, BioBERT Lee et al., 2020, SciBERT Beltagy et al., 2019, PubMedBERT Gu et al., 2021, and BioMegatron Shin et al., 2020 represent prominent encoder-based domain-adaptive pretraining efforts. In the clinical domain, ClinicalBERT Huang et al., 2019 and related work show that adapting pretrained models to clinical notes can improve performance on clinical prediction and classification. For broader medical language understanding, large-scale instruction tuning and multitask objectives have also been explored in the medical setting Jiang et al., 2023; Singhal et al., 2023.

Domain mismatch, limited labels, and privacy constraints complicate clinical NLP, making efficient adaptation strategies particularly important. Consequently, approaches that reduce the number of trainable parameters while maintaining task performance have become central to practical deployment in clinical contexts.

Parameter-Efficient Fine-Tuning and Computationally Efficient Adaptation

Full fine-tuning updates all parameters of a pretrained model and typically yields strong downstream performance, but it can be computationally expensive and memory intensive for large models. This motivates parameter-efficient fine-tuning (PEFT) methods that update only a small subset of parameters while keeping most pretrained weights frozen. Early and conceptually related ideas include updating only parts of a network, fine-tuning only higher layers, or using lightweight task-specific heads Howard and Ruder, 2018; Peters et al., 2019. More recent PEFT methods introduce structured low-rank or modular adaptations that are explicitly designed for large Transformers.

Adapter layers insert small bottleneck modules into each Transformer block, enabling efficient task adaptation with minimal additional parameters Houlsby et al., 2019; Pfeiffer et al., 2021. LoRA learns low-rank updates to attention and projection matrices without modifying the original weights, reducing memory usage and enabling efficient optimization Hu et al., 2022. Related low-rank or prompt-like approaches

include prefix tuning X. L. Li and Liang, 2021, prompt tuning Lester et al., 2021, and p-tuning variants X. Liu et al., 2021. BitFit shows that updating only bias terms can yield surprisingly strong performance in certain settings Zaken et al., 2022. IA³ and similar methods reparameterize intermediate activations or gates rather than updating full weight matrices H. Liu et al., 2022. Comprehensive surveys further systematize the PEFT landscape and clarify tradeoffs among methods Ding et al., 2023.

In parallel, optimization and regularization techniques have been developed to stabilize fine-tuning and improve generalization. AdamW decouples weight decay from gradient updates and is widely used in Transformer training Loshchilov and Hutter, 2019. Dropout remains a core regularization method to mitigate overfitting Srivastava et al., 2014. Weight tying between input embeddings and output projections is known to improve language modeling efficiency and can reduce parameter count Press and Wolf, 2017. These training principles and parameter-sharing strategies motivate careful parameter accounting and complexity analysis when proposing selective fine-tuning schemes.

The selective fine-tuning approach presented in this paper is aligned with this broader body of work. Rather than introducing new modules across all layers, training is restricted to the topmost GPT-2 block, along with the final normalization layer and the classification head. This design yields a clear reduction in backpropagation cost and trainable parameter count while retaining the representational capacity learned during pretraining.

Clinical NLP and Modeling Unstructured EHR Narratives

Clinical NLP aims to extract structured knowledge from unstructured clinical narratives and enable predictive modeling and decision support. Foundational resources and shared tasks such as i2b2 have accelerated progress by providing benchmark datasets for clinical concept extraction, relation extraction, and phenotyping Uzuner et al., 2011. More recent shared tasks and datasets have expanded evaluation to clinical temporal reasoning and other complex phenomena Huang et al., 2019; Mullenbach et al., 2018. Classic clinical corpora such as MIMIC have enabled broad research on clinical prediction and text-based risk modeling Johnson et al., 2016. Clinical text classification is often operationalized through coding tasks such as ICD assignment, where label spaces are large and notes are long F. Li and Yu, 2019; Mullenbach et al., 2018.

Transformer models have been widely applied to clinical NLP, often via encoder-based architectures due to their strong discriminative capabilities Devlin et al., 2019; Gu et al., 2021; Lee et al., 2020. However, decoder-only models are increasingly relevant for clinical note understanding because they can model long-form generation, reasoning, and context completion, and can be adapted for classification through lightweight heads. Empirical studies demonstrate that domain-adapted

language models improve downstream clinical tasks, but also highlight the tension between performance, compute, and data constraints in clinical settings Gu et al., 2021; Huang et al., 2019. Recent work on clinical and biomedical LLMs reflects growing interest in large-scale models for medical QA, reasoning, and summarization, while emphasizing safety and evaluation challenges Jiang et al., 2023; Singhal et al., 2023.

Overall, the literature supports three key conclusions relevant to this paper: (i) pretrained Transformers provide strong contextual representations for long and specialized text Devlin et al., 2019; Radford et al., 2019; Vaswani et al., 2017, (ii) domain adaptation and continued pretraining improve performance in biomedical and clinical NLP Gu et al., 2021; Gururangan et al., 2020; Huang et al., 2019; Lee et al., 2020, and (iii) parameter-efficient or selective fine-tuning is often necessary for practical deployment under limited compute and limited labeled data Houlsby et al., 2019; Hu et al., 2022; Lester et al., 2021; X. L. Li and Liang, 2021. These findings motivate the selective fine-tuning design and the explicit parameter and time-complexity analysis presented in this work.

Beyond full end-to-end fine-tuning, prior studies have shown that selectively updating subsets of model parameters can yield competitive performance while substantially reducing computational cost. Early analyses of transfer learning in deep neural networks indicate that higher layers tend to encode task-specific features, whereas lower layers capture more general linguistic representations Peters et al., 2019; Yosinski et al., 2014a. Motivated by these observations, several works have explored partial fine-tuning strategies for Transformer-based models, including freezing lower layers and updating only top layers or task-specific heads Howard and Ruder, 2018. More recent parameter-efficient fine-tuning approaches further formalize this idea by introducing lightweight adaptation mechanisms such as adapter modules, low-rank updates, or prompt-based reparameterization, enabling efficient downstream learning without modifying the full parameter set Houlsby et al., 2019; Hu et al., 2022; X. L. Li and Liang, 2021. These approaches are particularly relevant in domains such as clinical natural language processing, where labeled data and computational resources are often limited, and they motivate the selective fine-tuning strategy adopted in this work.

LLM Architecture to Support Classification

Overall GPT Model Architecture

This section presents the overall GPT architecture designed for the classification of unstructured clinical data, illustrating how the model components are integrated into a unified end-to-end system. The architecture is based on a decoder-only Transformer framework adapted to process and represent free-text clinical narratives in an autoregressive manner. Figure 1 provides a high-level overview of the complete model pipeline used for clinical text classification. In the following subsections, each major architectural component, including tokenization, embedding layers, masked self-attention blocks, feed-forward networks, and the classification head, is

described in detail.

Model Overview: The GPT model is a unidirectional (decoder-only) Transformer designed for autoregressive language modeling. Given an input sequence of length T , the model processes tokens sequentially while enforcing causal dependencies, ensuring that each token representation attends only to itself and preceding tokens in the sequence Radford et al., 2018, 2019; Vaswani et al., 2017.

Formally, an input token sequence is first mapped to a sequence of continuous vector representations by summing token embeddings and positional embeddings. This results in an embedding matrix $X \in \mathbb{R}^{T \times d_{model}}$,

where d_{model} denotes the model’s hidden dimensionality.

Embedding and Regularization: The combined token and positional embeddings are passed through an embedding-level dropout layer, which acts as an early regularization mechanism to reduce overfitting and improve generalization during training. This dropout is applied uniformly across all token positions in the sequence.

Stack of Decoder-only Transformer Blocks:

The regularized embeddings are then processed by a stack of N identical decoder-only Transformer blocks. Each block consists of two primary sublayers: (i) causal multi-head self-attention, and (ii) a position-wise feed-forward network (FFN).

Causal masking within the self-attention mechanism enforces the autoregressive constraint, preventing information flow from future tokens to past tokens. Residual connections and layer normalization within each block stabilize training and enable effective gradient propagation across deep architectures. The repeated stacking of these blocks allows the model to build progressively richer contextual representations over long sequences Vaswani et al., 2017.

Final Normalization and Output Projection: After passing through the full stack of Transformer blocks, the hidden representations are normalized using a final layer normalization layer. This normalization step stabilizes the hidden states before projection into the vocabulary space and has been shown to improve training dynamics in deep Transformer models Ba, Kiros, and Hinton, 2016; Xu et al., 2020.

The normalized representations are then fed into a linear output layer that projects each token’s hidden state into a vector of unnormalized scores (logits) over the vocabulary:

$\text{logits} \in \mathbb{R}^{T \times |V|}$, where $|V|$ denotes the vocabulary size. Each row of the logits matrix corresponds to the model’s prediction for the next token at a given position in the input sequence.

Autoregressive Prediction: During training, these logits are typically converted into probability distributions using a softmax function and optimized using a cross-entropy loss. During inference, the model generates text autoregressively by sampling or selecting the most probable token at each step and appending it to the input sequence, thereby extending the sequence one token at a time Brown et al., 2020; Radford et al., 2019.

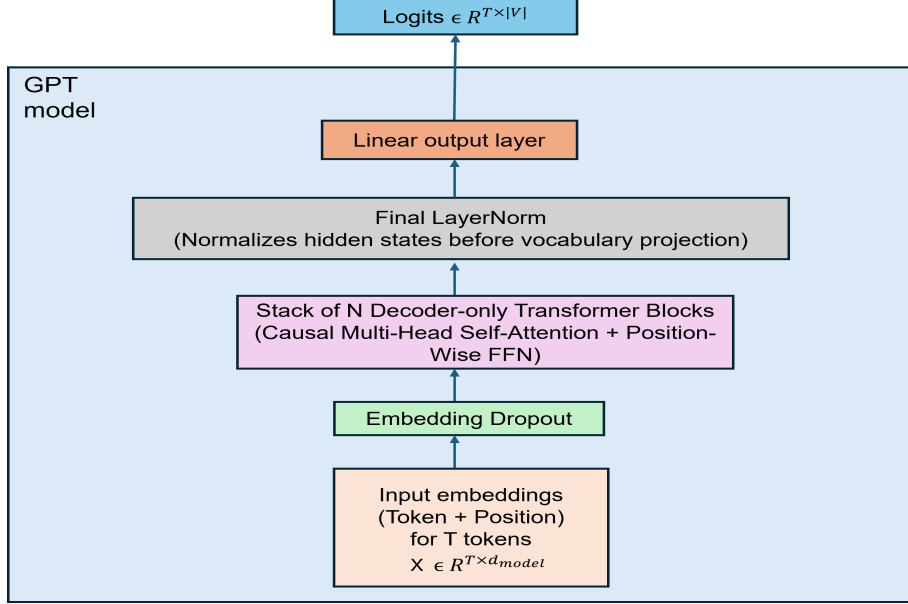


Figure 1: Overall architecture of the GPT model.

Input Pre-processing

The input pre-processing pipeline in Transformer-based language models shown in figure 2 begins with subword tokenization using byte pair encoding algorithm Gage, 1994; Sennrich et al., 2016, wherein raw text is segmented into a sequence of discrete tokens $x_1, x_2, x_3, \dots, x_n$ that serve as the fundamental units for embedding and downstream representation learning. Each token is then mapped to a continuous vector representation through a learned token embedding function $E(x_i)$. To encode word order information, a positional embedding $P(i)$, corresponding to the token’s position within the sequence, is added to the token embedding. The resulting input embedding is computed as $Z_i = E(x_i) + P(i)$ where the addition is performed element-wise. These input embeddings serve as the final representations passed to subsequent Transformer layers for contextual modeling.

Multi-Head Self-Attention Mechanism

The multi-head self-attention mechanism, including scaled dot-product attention, parallel attention heads, head concatenation, and the final output projection, was originally introduced by Vaswani et al., 2017 and forms the foundation of modern Transformer-based architectures.

Figure 3 illustrates the causal multi-head self-attention mechanism, a fundamental building block of Transformer-based language models. The figure depicts how a shared input embedding matrix is first mapped into query, key, and value representations through shared linear projections and then partitioned across multiple attention heads. Each head independently computes scaled dot-product attention, applies causal masking to prevent access to future tokens, and incorporates dropout for regularization. The resulting head-specific context vectors are subsequently concatenated and

passed through an output linear projection to produce the final multi-head attention representation.

1. Linear Projections into Queries, Keys, and Values: Within the multi-head attention block, the input embedding matrix Z is first transformed using three shared linear projections to obtain the query, key, and value representations, following the standard Transformer formulation introduced by Vaswani et al. Vaswani et al., 2017:

Query projection: $Q = ZW_Q$, Key projection: $K = ZW_K$, Value projection: $V = ZW_V$, where W_Q, W_K, W_V are learnable weight matrices shared across all attention heads. The resulting query, key, and value matrices are then reshaped and partitioned along the feature dimension into H parallel attention heads, such that each head $i \in \{1, 2, \dots, H\}$ operates on a subspace of dimension $d_K = d_{model} \div H$. In practice, this partitioning is implemented via tensor reshaping rather than explicit slicing. This yields head-specific representations Q_i, K_i, V_i without requiring separate projection matrices per head, as commonly implemented in modern deep learning frameworks Paszke et al., 2019; Vaswani et al., 2017.

This shared-projection design improves computational efficiency while still allowing each head to attend to different representation subspaces. Figure 3 illustrates this process by showing a single shared projection block feeding multiple attention heads in parallel via dashed connections.

2. Scaled Dot-Product Attention Within Each Head: For each head, the queries, keys, and values are used to compute attention outputs through a scaled dot-product attention operation originally proposed in Vaswani et al., 2017. This involves the following steps:

Attention score computation: The raw attention score matrix is obtained by taking the dot product between the queries and the transposed keys. $S_i = Q_i K_i^T$. This yields a score for

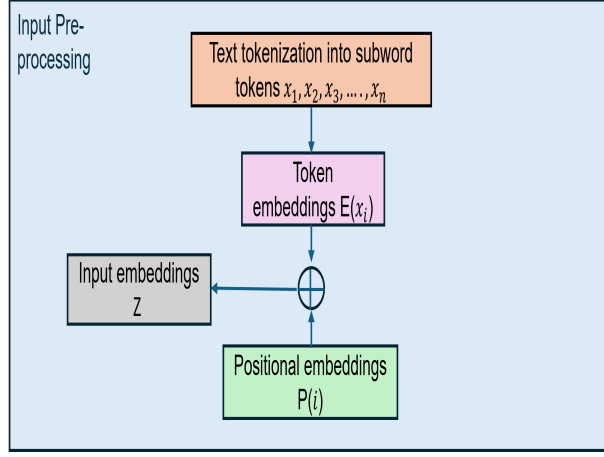


Figure 2: Input Pre-Processing and Embedding Construction in Transformer-Based Language Models.

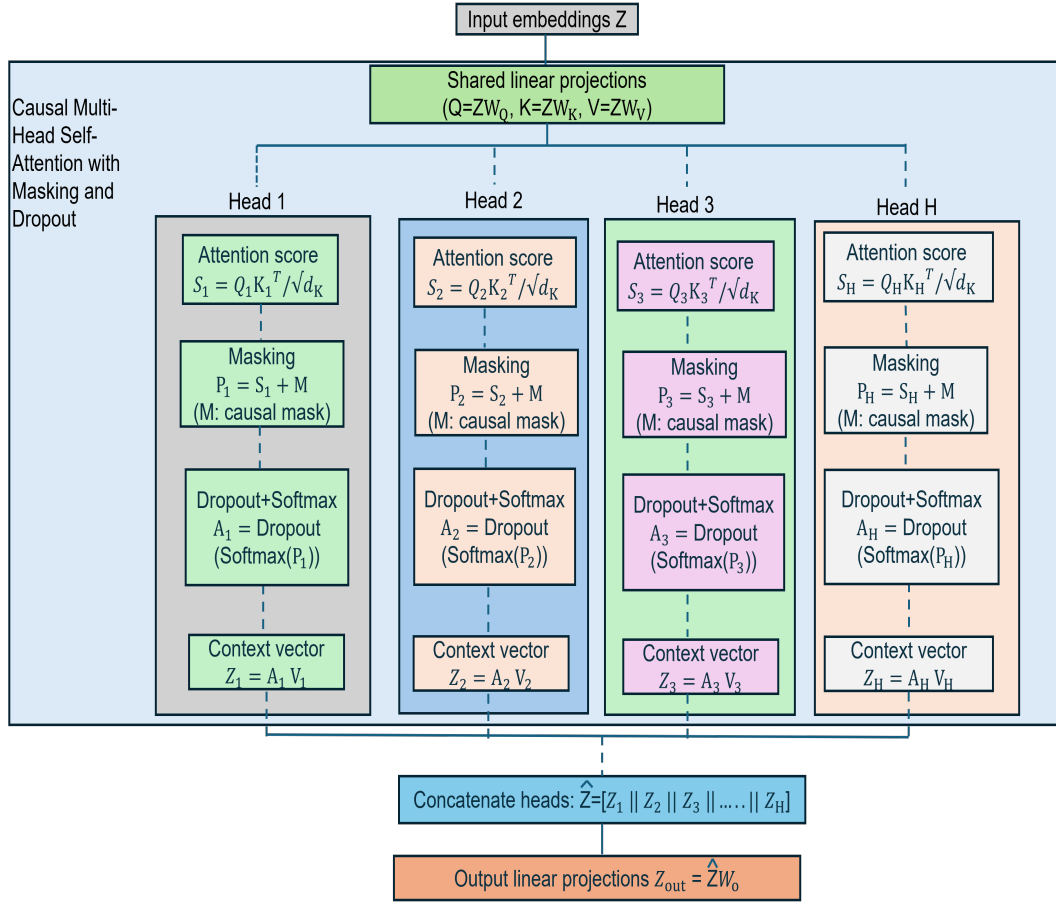


Figure 3: Computation Flow of Causal Multi-Head Self-Attention with Scaled Dot-Product Attention, Masking, and Dropout.

how much each position should attend to every other position:

Scaling: The raw scores are scaled by the inverse square root of the key dimension, which stabilizes gradients during training:

$$\tilde{S}_i = \frac{S_i}{\sqrt{d_K}},$$

where d_K denotes the dimensionality of the key vectors. After scaling and causal masking, a softmax function is applied along the last axis to normalize the attention scores into a probability distribution over tokens. After scaling and causal masking, a softmax function is applied along the last axis to normalize the attention scores into a probability distribution over tokens:

$$A_i = \text{Softmax}(P_i),$$

where each row of A_i sums to one and represents the relative importance assigned to all valid (non-masked) tokens for a given query position Vaswani et al., 2017.

3. Causal Masking and Dropout: To enforce the autoregressive property required for causal language modeling, a causal (masked) self-attention mechanism is employed, following the design introduced in generative pre-trained Transformer models Radford et al., 2018, 2019 to the scaled attention scores before normalization. This mask assigns large negative values to positions corresponding to future tokens, preventing each position from attending to subsequent positions in the sequence: $P_i = \tilde{S}_i + M$. Here, M denotes a causal upper-triangular mask with $-\infty$ entries assigned to future positions, ensuring autoregressive behavior. Following masking, a softmax function converts the masked scores into attention weights, and dropout is applied to improve regularization: $A_i = \text{Dropout}(\text{Softmax}(P_i))$.

4. Context Vector Computation: The normalized attention weights are then used to compute the context vector for each head as a weighted sum of the value vectors:

$$Z_i = A_i V_i.$$

Each head produces its own context tensor Z_i , capturing information from the input sequence according to distinct attention patterns. Figure 3 depicts these operations beneath each head, explicitly illustrating the attention score computation, masking, softmax, dropout, and context vector formation.

5. Parallelism across Multiple Heads: Unlike single-head attention, the above sequence of operations is executed in parallel across H heads. While all heads share the same input embeddings, each head attends to a different subspace of the shared projected representations, enabling the model to capture diverse syntactic, semantic, and positional relationships simultaneously Vaswani et al., 2017.

The figure 3 emphasizes this parallel structure by visually separating the computations for each head while maintaining a shared input.

Finally, the concatenated representation is passed through an output linear projection W_o to mix information across heads and prepare the output for subsequent Transformer layers. In the figure 3, this is shown as the bottom block labeled Output Linear Projections.

6. Concatenation and Output Projection: After all heads compute their respective context vectors $Z_1, Z_2, Z_3, \dots, Z_H$, these vectors are concatenated along the feature dimension: $\hat{Z} = [Z_1 \parallel Z_2 \parallel \dots \parallel Z_H]$.

The concatenated tensor is then passed through a final output linear projection: $Z_{out} = \hat{Z} W_o$, where W_o is a learnable weight matrix that mixes information across heads and produces the output representation used by subsequent Transformer layers. This operation is shown at the bottom of Figure 3 as the Output linear projection block Paszke et al., 2019; Vaswani et al., 2017.

This formulation closely follows standard implementations of multi-head self-attention used in modern deep learning frameworks, including PyTorch’s `nn.MultiheadAttention`, where query, key, and value projections are typically computed using a fused linear layer and the outputs of all heads are combined through a final projection Paszke et al., 2019. The inclusion of causal masking and dropout aligns the architecture with commonly used Transformer-based language models.

Transformer

In decoder-only Transformer architectures, such as GPT-2, causal masking is a fundamental design principle that enables autoregressive sequence modeling Radford et al., 2019. In these models, each Transformer block processes an input sequence through a series of structured operations designed to capture contextual dependencies while preserving the left-to-right generation constraint. As illustrated in Figure 4, each block consists of two main sublayers: a masked multi-head self-attention sublayer and a position-wise feed-forward sublayer. Each sublayer is wrapped with layer normalization, dropout, and residual connections.

Layer Normalization (Pre-Norm): At first, layer normalization is applied to the input $X_{LN} = LN(X)$. This pre-normalization stabilizes training by mitigating internal covariate shift, a phenomenon in deep neural networks in which the distribution of inputs to hidden layers changes as preceding layers are updated during training. By reducing such distributional drift, pre-normalization accelerates convergence and improves optimization stability by alleviating vanishing and exploding gradient issues. As a result, this design is widely adopted in modern large language models Xu et al., 2020. The core principle of pre-normalization is to normalize neural activations to have zero mean and unit variance prior to subsequent transformations.

Masked Multi-Head Self-Attention: The normalized representations are passed to a masked multi-head self-attention (MHA) sublayer: $A = MHA(X_{LN})$.

Causal masking is applied within the attention mechanism to prevent each token from attending to future positions, ensuring autoregressive behavior consistent with decoder-style language models Radford et al., 2019; Vaswani et al., 2017.

Dropout and Residual Connection (Attention Sublayer): Dropout is applied to the output of the masked multi-head

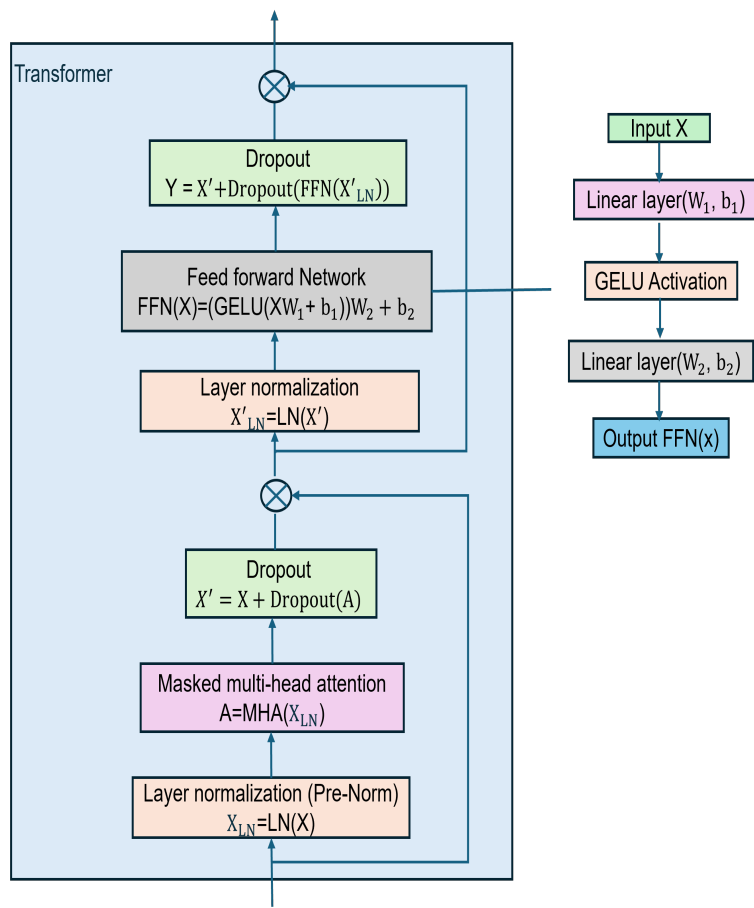


Figure 4: Decoder-only Transformer block with pre-normalization, masked multi-head self-attention, residual connections, dropout, and a position-wise feed-forward network.

self-attention sublayer to mitigate overfitting by randomly deactivating a subset of attention activations during training. The regularized attention output is then combined with the original input through a residual (skip) connection: $X' = X + \text{Dropout}(A)$. This residual connection enables the direct propagation of information from earlier layers to later layers, facilitating more effective gradient flow during back-propagation. By providing an identity mapping path, residual connections alleviate vanishing gradient issues, accelerate convergence, and improve optimization stability in deep neural networks He et al., 2016. In the context of Transformer architectures, this mechanism allows each layer to refine representations incrementally while preserving previously learned contextual information.

Layer Normalization Before Feed-Forward Network: The intermediate representation is again normalized prior to the feed-forward network: $X'_{LN} = LN(X')$.

Position-Wise Feed-Forward Network: A position-wise feed-forward network (FFN) is applied independently to each token representation produced by the self-attention sublayer. This component is implemented as a two-layer fully connected neural network with a single non-linear activation function applied element-wise between the layers. The first linear transformation projects the input representation into a higher-dimensional feature space, enabling the model to capture richer and more expressive patterns through an expanded set of parameters. This expansion layer increases the model’s capacity to learn complex relationships among features that may not be adequately represented in the original embedding space.

The second linear transformation subsequently projects the activated representations back to the original model dimension. This contraction step ensures that the input and output dimensions of the Transformer block remain consistent, which is essential for scalability, residual connections, and efficient stacking of multiple layers. By combining dimensional expansion, non-linear transformation, and dimensional reduction, the FFN significantly enhances the representational power of the Transformer while maintaining architectural compatibility across layers Vaswani et al., 2017. In modern Transformer-based language models, the Gaussian Error Linear Unit (GELU) is commonly used as the activation function due to its smooth non-linear behavior and improved empirical performance Devlin et al., 2019; Hendrycks and Gimpel, 2016. For an input token representation $x \in \mathbb{R}^{d_{\text{model}}}$, the FFN is defined as:

$FFN(X) = (\text{GELU}(XW_1 + b_1))W_2 + b_2$, where W_1 and W_2 are learnable weight matrices, and b_1 and b_2 are learnable bias vectors. The first linear transformation projects the input from the model dimension d_{model} to a higher-dimensional hidden space, often denoted as d_{ff} , enabling richer feature extraction. The GELU activation function introduces non-linearity by modulating inputs according to their magnitude and sign, allowing the network to selectively pass or suppress information in a smooth and probabilistic manner. The GELU activation

is formally defined as Hendrycks and Gimpel, 2016:

$$\text{GELU}(x) = x \Phi(x),$$

where $\Phi(x)$ denotes the cumulative distribution function of the standard normal distribution. In practice, an efficient approximation is often used:

$$\text{GELU}(x) \approx 0.5x \left(1 + \tanh \left[\sqrt{\frac{2}{\pi}} \left(x + 0.044715x^3 \right) \right] \right).$$

Because the FFN is applied position-wise, the same parameters (W_1, b_1, W_2, b_2) are shared across all token positions, and each token is transformed independently. As a result, cross-token interactions are handled by the self-attention mechanism, while the FFN enhances the expressive power of individual token representations through non-linear feature transformation Vaswani et al., 2017.

Dropout and Residual Connection (Feed-Forward Sub-layer): Dropout is applied to the FFN output, followed by another residual connection:

$$Y = X' + \text{Dropout}(FFN(X'_{LN})).$$

The output Y serves as the final representation produced by the Transformer block.

Stacking of Transformer Blocks: Multiple Transformer blocks are stacked sequentially, enabling the model to learn increasingly abstract and context-rich representations Brown et al., 2020; Radford et al., 2019. The output of the final block is passed to downstream components such as pooling layers or classification heads.

Classification Head Using Last-Token Representation

In decoder-only GPT architectures, sequence-level representations for classification can be derived directly from the hidden state of the final token. Due to the causal self-attention mechanism, the representation of the last token implicitly encodes contextual information from all preceding tokens in the input sequence. This property makes the last-token hidden state a natural and computationally efficient choice for unstructured clinical text classification.

Let $H \in \mathbb{R}^{T \times d_{\text{model}}}$ denote the output of the final Transformer block for an input sequence of length T , where d_{model} is the hidden dimensionality. The sequence representation is obtained by selecting the hidden state corresponding to the final token:

$$h_{\text{seq}} = h_T \in \mathbb{R}^{d_{\text{model}}}.$$

This last-token representation serves as a compact summary of the entire clinical narrative, leveraging the autoregressive dependency structure of the model. Unlike encoder-based architectures that rely on a dedicated classification token, decoder-only models naturally accumulate contextual information into the final token representation. A linear classification head is applied to h_{seq} to produce prediction logits:

$$\mathbf{z} = Wh_T + b,$$

where $W \in \mathbb{R}^{C \times d_{\text{model}}}$ and $b \in \mathbb{R}^C$ are learnable parameters, and C denotes the number of output labels.

Binary Classification Head (Single-Label): For binary clinical prediction tasks (e.g., presence vs. absence of any abnormality), the model outputs a single logit ($C = 1$):

$$z = w^\top h_T + b,$$

where $w \in \mathbb{R}^{d_{\text{model}}}$ and $b \in \mathbb{R}$.

The predicted probability of the positive class is obtained using the sigmoid function:

$$P(y = 1 | x) = \sigma(z) = \frac{1}{1 + \exp(-z)}.$$

During supervised training, the model is optimized using binary cross-entropy loss:

$$\mathcal{L}_{\text{bin}} = -[y \log \sigma(z) + (1 - y) \log(1 - \sigma(z))],$$

where $y \in \{0, 1\}$ is the ground-truth label. Gradients from the binary classification objective are backpropagated through the classification head and the full Transformer stack, enabling the model to learn discriminative clinical representations.

Multi-Label Classification Head (CheXpert-Style Labels): For multi-label clinical classification tasks, multiple findings may co-occur in the same note (e.g., edema and pleural effusion). Therefore, each label is treated as an independent binary output. In this setting, the classification head produces a vector of logits $\mathbf{z} \in \mathbb{R}^C$:

$$\mathbf{z} = Wh_T + b,$$

where C is the total number of clinical labels. The probability of each label c being present is computed using an element-wise sigmoid:

$$P(y_c = 1 | x) = \sigma(z_c), \quad c \in \{1, \dots, C\}.$$

Training is performed using a multi-label binary cross-entropy objective (often implemented as `BCEWithLogitsLoss`, defined as:

$$\mathcal{L}_{\text{multi}} = -\sum_{c=1}^C [y_c \log \sigma(z_c) + (1 - y_c) \log(1 - \sigma(z_c))],$$

where $\mathbf{y} = (y_1, \dots, y_C) \in \{0, 1\}^C$ denotes the ground-truth multi-label vector.

By relying on the last-token representation h_T , this unified strategy preserves the architectural simplicity of GPT-style models while supporting both binary and multi-label clinical prediction tasks on long and unstructured radiology narratives.

Pretraining and Initialization from OpenAI Open-Weight Checkpoints

GPT-style decoder-only Transformer models are originally pretrained using a self-supervised autoregressive language modeling objective. Given a tokenized input sequence

$x_{1:T} = (x_1, \dots, x_T)$, the model is trained to maximize the conditional likelihood of each token given all previous tokens:

$$\log p_\theta(x_{1:T}) = \sum_{t=1}^T \log p_\theta(x_t | x_{<t}),$$

which is optimized via cross-entropy loss over large-scale unlabeled text corpora Brown et al., 2020; Radford et al., 2019. This pretraining procedure enables the model to learn general-purpose syntactic and semantic representations that can be transferred to a wide range of downstream tasks.

In this work, large-scale language model pretraining is not performed from scratch. Instead, a transfer learning strategy is adopted by initializing the Transformer backbone using publicly released *open-weight* pretrained checkpoints provided by OpenAI. Specifically, pretrained parameters θ_0 are loaded from an OpenAI-released GPT checkpoint (e.g., GPT-2), including the token embedding layer, positional embeddings, and the full stack of masked self-attention and feed-forward blocks OpenAI, 2019; Radford et al., 2019. These pretrained weights serve as the starting point for subsequent task adaptation.

After loading the pretrained checkpoint, the Transformer backbone is used as an initialization for downstream task adaptation. This initialization strategy substantially reduces computational cost compared to training from scratch and improves sample efficiency by leveraging linguistic knowledge acquired during large-scale pretraining. Prior studies have demonstrated that such transfer learning approaches are particularly effective for domain-specific natural language processing tasks, including those involving long and unstructured clinical narratives Devlin et al., 2019; Huang et al., 2019.

Overall, initializing the proposed architecture from OpenAI’s open-weight pretrained models enables efficient domain adaptation while preserving the strong contextual representation capabilities learned during pretraining. Details of the supervised optimization procedure for clinical classification are described in the subsequent fine-tuning section.

Step-by-Step Selective Fine-Tuning Procedure (with Accuracy-Oriented Evaluation)

Starting from the pretrained initialization described in previous section, the model is fine-tuned for supervised clinical text classification.

Figure 5 summarizes the supervised fine-tuning workflow used to adapt a pretrained GPT model for sequence classification while updating only a small subset of parameters. Training is conducted for a fixed number of epochs over the fine-tuning dataset. Although Figure 5 includes a convergence check for completeness, this check is used only to monitor the stabilization of the validation loss and does not replace the epoch-based stopping criterion. This formulation reflects common practice in Transformer fine-tuning, where a predefined number of epochs is used while convergence indicators are tracked for diagnostic purposes. This section explains each step in detail and clarifies how selective fine-tuning reduces

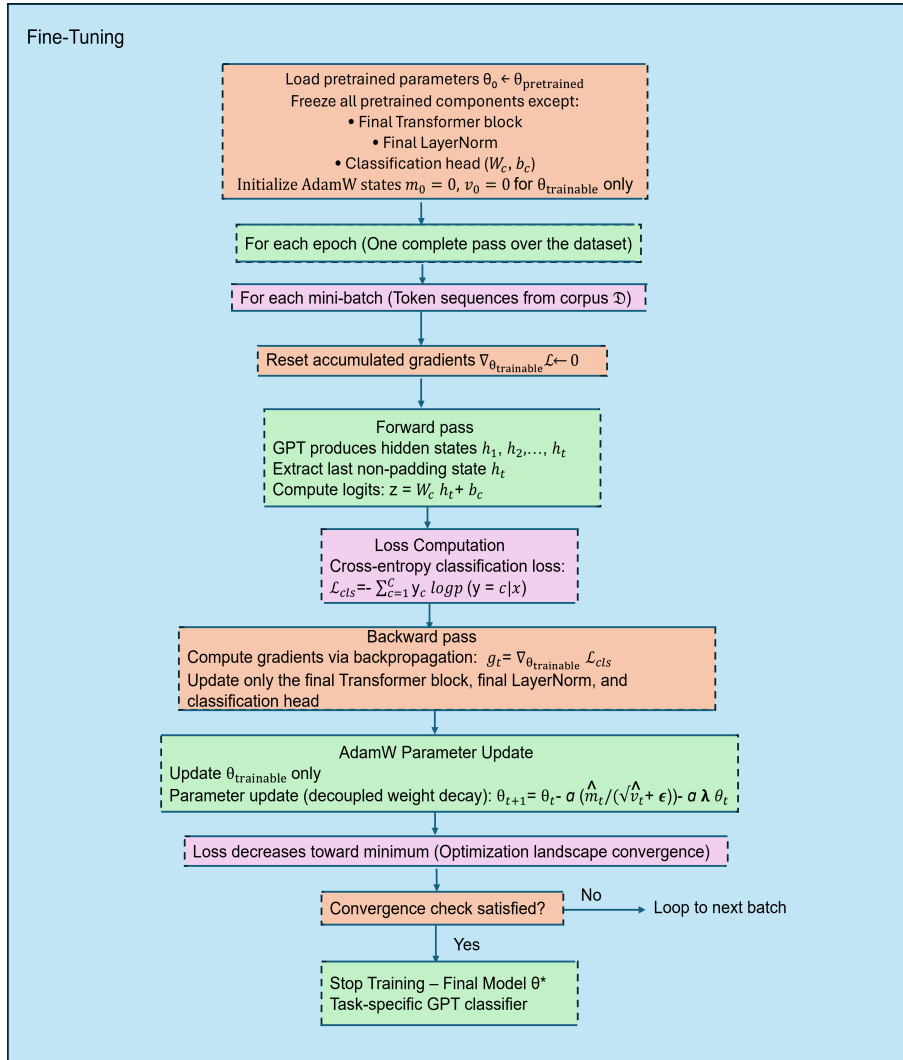


Figure 5: Selective fine-tuning workflow for a GPT-based classification model. Pretrained parameters are loaded and all layers are frozen except the final Transformer block, final LayerNorm, and the task-specific classification head. Fine-tuning proceeds over mini-batches using cross-entropy loss and AdamW updates applied only to trainable parameters, yielding a task-specific GPT classifier.

computation and overfitting risk while preserving general language representations learned during pretraining Peters et al., 2019; Radford et al., 2019; Vaswani et al., 2017.

A pretrained GPT-based language model is fine-tuned to perform sequence-level classification tasks on labeled clinical text. Fine-tuning adapts a model pretrained on large-scale unlabeled corpora to a downstream supervised task, avoiding the need to train all parameters from scratch while leveraging pretrained linguistic representations.

Given a labeled dataset

$$\mathcal{D} = \{(x^{(i)}, y^{(i)})\}_{i=1}^N,$$

each input sequence $x^{(i)} = (x_1, x_2, \dots, x_T)$ consists of a variable-length token sequence, and $y^{(i)}$ denotes the corresponding class label.

Input Representation and Data Loader: Each input sequence is tokenized using the GPT tokenizer and converted into a fixed-length representation through truncation and padding. Sequences exceeding the maximum context length are truncated, while shorter sequences are padded using a designated padding token. This preprocessing enables efficient mini-batch training and is standard practice in Transformer-based models Wolf et al., 2020.

A data loader groups tokenized sequences into mini-batches and produces attention masks that distinguish valid tokens from padding tokens. For a mini-batch of size B , the data loader outputs an input tensor $\mathbf{X} \in \mathbb{R}^{B \times T}$, an attention mask $\mathbf{M} \in \{0, 1\}^{B \times T}$, and a label vector $\mathbf{y} \in \mathbb{R}^B$.

Step 1: Load pretrained parameters Fine-tuning begins by initializing model parameters from a pretrained checkpoint:

$$\theta_0 \leftarrow \theta_{\text{pretrained}}.$$

This step transfers general linguistic knowledge learned from large-scale self-supervised training to the downstream clinical classification task, which is a standard transfer-learning strategy for Transformer language models Devlin et al., 2019; Radford et al., 2019.

Step 2: Freeze all parameters except the final block, final LayerNorm, and classification head In this work, all pretrained parameters are frozen except: (i) the final Transformer block, (ii) the final layer normalization module, and (iii) the task-specific classification head (W_c, b_c). Formally, let $\theta = \{\theta_{\text{frozen}}, \theta_{\text{trainable}}\}$, where

$$\theta_{\text{trainable}} = \{\theta_{\text{block-}L}, \theta_{\text{LN-final}}, W_c, b_c\}.$$

During optimization, gradients are computed and applied only to $\theta_{\text{trainable}}$. This selective strategy is motivated by evidence that higher Transformer layers tend to capture more task-specific representations, whereas lower layers encode more general and transferable features Peters et al., 2019; Yosinski et al., 2014a.

Step 3: Initialize the classification head For C classes, a linear classification head is attached to the final sequence representation:

$$\mathbf{z} = W_c h_T + b_c,$$

where $W_c \in \mathbb{R}^{C \times d_{\text{model}}}$ and $b_c \in \mathbb{R}^C$ are trainable parameters. This head maps the final hidden representation to class logits and is standard for Transformer-based classification systems Devlin et al., 2019.

Step 4: Iterate over epochs Training proceeds for a fixed number of epochs, where each epoch represents one full pass over the labeled training data. Epoch-based training is standard in deep learning optimization and enables stable learning rate scheduling and progress monitoring Goodfellow et al., 2016.

Step 5: Iterate over mini-batches using a data loader The dataset is processed in mini-batches to improve computational efficiency and memory usage. A data loader produces batches of:

$$(\mathbf{X}, \mathbf{M}, \mathbf{y}),$$

where \mathbf{X} contains token IDs, \mathbf{M} is an attention mask that distinguishes valid tokens from padding, and \mathbf{y} contains the ground-truth labels. Mini-batch training is standard for stochastic optimization and is the default practice in modern deep learning frameworks Paszke et al., 2019.

Step 6: Reset accumulated gradients Before each parameter update, gradients are reset:

$$\nabla \theta_{\text{trainable}} \leftarrow 0.$$

This prevents unintended accumulation of gradients across batches, which would otherwise distort the optimization step and lead to incorrect parameter updates Paszke et al., 2019.

Step 7: Forward pass through frozen and trainable components Each mini-batch is passed through the GPT model. Frozen components (embeddings and earlier Transformer blocks) compute representations but do not receive gradient updates. The final Transformer block and final LayerNorm remain trainable and adapt to the downstream task. The model outputs hidden states:

$$\mathbf{H} = (h_1, h_2, \dots, h_T),$$

where causal self-attention ensures that h_t depends only on tokens up to position t Radford et al., 2019; Vaswani et al., 2017.

Step 8: Extract the last non-padding hidden state Because GPT is decoder-only and does not include a dedicated classification token (e.g., [CLS]), the final hidden state corresponding to the last non-padding token, denoted h_T is used. This choice is principled because the last state has integrated information from the full preceding context under causal attention, making it a natural sequence-level representation for classification Radford et al., 2019.

Step 9: Compute logits and supervised loss Class logits are computed with the classification head and converted to probabilities via softmax:

$$p(y = c | x) = \frac{\exp(z_c)}{\sum_{j=1}^C \exp(z_j)}.$$

The supervised objective is the cross-entropy loss:

$$\mathcal{L}_{\text{cls}} = - \sum_{c=1}^C y_c \log p(y = c | x),$$

which is the standard loss for multi-class classification Bishop, 2006; Goodfellow et al., 2016.

Step 10: Backward pass restricted to trainable parameters Gradients are computed by backpropagation:

$$g_t = \nabla_{\theta_{\text{trainable}}} \mathcal{L}_{\text{cls}},$$

and flow only through the final block, final LayerNorm, and the classification head. Freezing the remaining layers prevents updates to general language representations and reduces overfitting risk when labeled data are limited Peters et al., 2019; Yosinski et al., 2014a.

Step 11: Update trainable parameters using AdamW

Only $\theta_{\text{trainable}}$ is updated using AdamW, which decouples weight decay from the gradient-based update and is commonly used for Transformer fine-tuning:

$$\theta_{\text{trainable}} \leftarrow \theta_{\text{trainable}} - \alpha \text{AdamW}(g_t).$$

where α denotes the learning rate. AdamW is widely adopted in modern NLP training and is specifically recommended for Transformer optimization Loshchilov and Hutter, 2019.

Step 12: Monitor training and validation performance (loss and accuracy) During training, the training loss is tracked, and evaluation on a validation set is performed optionally. Accuracy is computed as:

$$\text{Accuracy} = \frac{1}{N} \sum_{i=1}^N \mathbb{I}(\hat{y}_i = y_i), \quad \hat{y}_i = \arg \max_c z_{i,c}.$$

This provides an interpretable measure of classification performance and supports early stopping or model selection when validation accuracy plateaus Bishop, 2006; Goodfellow et al., 2016.

Step 13: Convergence check and final model Training is performed for a fixed number of epochs, after which the resulting parameters define the fine-tuned classifier:

$$\theta^* = \arg \min_{\theta_{\text{trainable}}} \mathcal{L}_{\text{cls}},$$

where only the selected modules have been adapted. This yields a task-specialized GPT-based classifier while preserving pretrained knowledge in frozen components Peters et al., 2019; Radford et al., 2019.

Selective Fine-Tuning Parameterization and Time Complexity Analysis

This section explains, in detail, how selective fine-tuning is performed in the GPT-2-based model and why this strategy substantially reduces computational cost. The explanation is written to be accessible to readers who may be new to large language models and Transformer architectures.

Overview of the Fine-Tuning Strategy

The fine-tuned model is derived from the GPT-2 decoder-only Transformer architecture described in the previous section. At a high level, GPT-2 consists of three main components: (i) an embedding layer that converts discrete tokens into continuous vectors, (ii) a stack of Transformer blocks that progressively refine contextual representations, and (iii) a final normalization stage prior to output generation Radford et al., 2019.

In standard full fine-tuning, all parameters of the model are updated using task-specific labeled data. However, GPT-2 contains over one hundred million parameters, making full fine-tuning computationally expensive and prone to overfitting when labeled data are limited. To address this, a *selective fine-tuning* strategy is adopted in which most pretrained parameters are frozen. Specifically, all parameters are frozen except those in the final Transformer block, the final layer normalization, and the task-specific classification head. The remainder of this section explains this design choice and its implications for parameter count and training-time complexity.

Frozen Components and Parameter Accounting

The proposed model adopts a selective fine-tuning strategy based on GPT-2 (small), in which the embedding layers and the lower Transformer blocks are kept fixed during task-specific training. This design leverages the strong general-purpose representations learned during large-scale pretraining, while substantially reducing optimization cost and memory requirements during fine-tuning.

Embedding Layers: GPT-2 includes a learned token embedding matrix $\mathbf{W}_{\text{te}} \in \mathbb{R}^{V \times d_{\text{model}}}$, which maps each token in the vocabulary to a continuous vector representation, and a learned positional embedding matrix $\mathbf{W}_{\text{pe}} \in \mathbb{R}^{T_{\text{max}} \times d_{\text{model}}}$, which encodes absolute token positions within the input sequence Radford et al., 2019. These embeddings capture general lexical semantics and positional structure and are shared across all downstream tasks.

In the GPT-2 (small) configuration, the hidden dimension is $d_{\text{model}} = 768$, the vocabulary size is $V = 50,257$, and the maximum context length is $T_{\text{max}} = 1024$. The total number of embedding parameters is therefore

$$\underbrace{50,257 \times 768}_{\text{token embeddings}} + \underbrace{1024 \times 768}_{\text{positional embeddings}} = 38,597,376 \approx 38.6 \text{ million.}$$

During selective fine-tuning, both embedding matrices are frozen. They participate in forward propagation by producing

input representations of shape $\mathbb{R}^{B \times T \times 768}$, where B is the batch size and T is the sequence length, but no gradients are computed or stored for these parameters during backpropagation.

Frozen Transformer Blocks: Following the embedding layer, GPT-2 consists of a stack of $L = 12$ decoder-only Transformer blocks Brown et al., 2020; Radford et al., 2019. Each block refines token representations using masked self-attention and position-wise feed-forward transformations. In the proposed setup, the first $L - 1 = 11$ Transformer blocks are frozen, while only the final block and task-specific head remain trainable.

Transformer Block Parameterization: Each Transformer block operates at hidden dimension $d_{\text{model}} = 768$ and uses $h = 12$ attention heads, yielding per-head dimensions $d_k = d_v = 64$, consistent with the original Transformer architecture Vaswani et al., 2017.

Multi-Head Self-Attention: The self-attention sublayer contains learned linear projections for queries, keys, and values, as well as an output projection:

$$\mathbf{W}_Q, \mathbf{W}_K, \mathbf{W}_V, \mathbf{W}_O \in \mathbb{R}^{768 \times 768}.$$

The total number of parameters in the attention sublayer is

$$4 \times 768 \times 768 = 2,359,296.$$

Feed-Forward Network: The feed-forward network expands the hidden dimension by a factor of four, $d_{\text{ff}} = 3,072$, and applies two linear transformations:

$$\mathbf{W}_1 \in \mathbb{R}^{768 \times 3,072}, \quad \mathbf{W}_2 \in \mathbb{R}^{3,072 \times 768}.$$

This sublayer contains

$$768 \times 3,072 + 3,072 \times 768 = 4,718,592$$

parameters.

Layer Normalization: Each Transformer block includes two Layer Normalization layers, each with a learnable scale and bias of size 768 Ba, Kiros, and Hinton, 2016. The total number of LayerNorm parameters per block is

$$2 \times 2 \times 768 = 3,072.$$

Total Parameters per Transformer Block: Summing all components, the total number of parameters in a single GPT-2 (small) Transformer block is

$$2,359,296 + 4,718,592 + 3,072 = 7,080,960 \approx 7.08 \text{ million.}$$

With 11 frozen Transformer blocks, this corresponds to approximately

$$11 \times 7.08 \text{ million} \approx 77.9 \text{ million}$$

frozen parameters.

Overall Frozen Parameter Count: Combining the frozen embedding layers (≈ 38.6 million parameters) and the first 11 frozen Transformer blocks (≈ 77.9 million parameters), the total number of frozen parameters is approximately

$$116.5 \text{ million.}$$

Although these components actively participate in forward propagation and generate contextualized representations of shape $\mathbb{R}^{B \times T \times 768}$, they incur no gradient computation or optimizer updates during backpropagation. This selective freezing strategy substantially reduces training-time memory usage and optimization overhead, while preserving the rich linguistic and contextual knowledge acquired during pretraining. Such behavior aligns with established transfer learning principles, where lower layers capture general-purpose features that transfer effectively across tasks Howard and Ruder, 2018.

Trainable Final Transformer Block

The only Transformer block that remains trainable is the *final* block in the stack (i.e., block L). This block is the topmost block in the architecture and directly precedes the final layer normalization and classification head. The final Transformer block produces the most abstract and task-specific representations, making it the most effective location for domain adaptation Peters et al., 2019; Yosinski et al., 2014a.

Each Transformer block contains two major subcomponents: a multi-head self-attention module and a position-wise feed-forward network. For a hidden dimension $d_{\text{model}} = 768$ and a feed-forward dimension $d_{\text{ff}} = 3072$, the parameter count can be understood as follows.

The self-attention module requires four linear transformations: three to generate the query, key, and value representations, and one additional projection applied after attention outputs are concatenated. Each of these transformations maps from d_{model} to d_{model} , resulting in a total of $4d_{\text{model}}^2 = 4 \times 768^2 \approx 2.36$ million parameters. The feed-forward network consists of two linear layers, one expanding the representation from d_{model} to d_{ff} , and one projecting it back. This contributes $2(d_{\text{model}} \times d_{\text{ff}}) = 2 \times (768 \times 3072) \approx 4.72$ million parameters. Together, the final Transformer block contains approximately 7.08 million trainable parameters.

From a time-complexity perspective, this block dominates the fine-tuning cost. For an input sequence of length T , the self-attention mechanism scales as $O(T^2 d_{\text{model}})$ due to pairwise interactions between tokens, while the feed-forward network scales as $O(T d_{\text{model}} d_{\text{ff}})$. Because backpropagation is restricted to a single Transformer block, the overall training-time complexity is substantially lower than that of full-model fine-tuning, which would require gradient computation through all L blocks Gururangan et al., 2020.

Trainable Final Layer Normalization

After the Transformer stack, GPT-2 applies a final layer normalization operation Ba, Kiros, and Hinton, 2016. This layer includes a learnable scale parameter γ_{final} and a learnable shift parameter β_{final} , each of dimension d_{model} . As a

result, this component introduces $2d_{\text{model}} = 1,536$ trainable parameters. The computational cost of layer normalization scales as $O(Td_{\text{model}})$ and is negligible compared to the cost of self-attention and feed-forward operations.

Trainable Classification Head

To adapt GPT-2 for supervised classification, a task-specific classification head is appended to the final hidden representation. This head consists of a linear projection with weight matrix $\mathbf{W}_{\text{cls}} \in \mathbb{R}^{d_{\text{model}} \times C}$ and bias vector $\mathbf{b}_{\text{cls}} \in \mathbb{R}^C$, where C is the number of output classes. For binary classification ($C = 2$), this results in $768 \times 2 + 2 = 1,538$ trainable parameters. The time complexity of this layer scales as $O(Td_{\text{model}}C)$ and is negligible relative to the Transformer block, as is typical in Transformer-based classification models Devlin et al., 2019.

Overall Trainable Parameter Count and Reduction

Under this selective fine-tuning strategy, the total number of trainable parameters is dominated by the final Transformer block. Specifically, approximately 7.08 million parameters are trainable in the final block, with an additional 0.0015 million parameters each from the final layer normalization and the classification head. In total, this yields roughly 7.08 million trainable parameters.

Compared to the full GPT-2 (small) model, which contains approximately 124 million parameters Radford et al., 2019, this represents a reduction of more than 94% in the number of parameters updated during training.

Implications for Training Efficiency

By restricting gradient updates to the final Transformer block and lightweight task-specific layers, the fine-tuning process significantly reduces both training time and memory consumption. This selective optimization approach enables efficient domain adaptation while preserving the general linguistic knowledge acquired during large-scale pretraining, making it particularly well suited for clinical and other low-resource text classification tasks Gururangan et al., 2020.

Dataset and Label Construction

The experiments in this study were conducted using the MIMIC-IV-Note database, a large-scale, de-identified clinical text corpus released through PhysioNet Goldberger et al., 2000. MIMIC-IV contains electronic health records associated with patients admitted to intensive care units and hospital wards at the Beth Israel Deaconess Medical Center, spanning more than a decade of clinical care Johnson et al., 2023. The dataset includes a wide range of unstructured clinical notes, such as discharge summaries, radiology reports, nursing notes, and physician documentation, which reflect real-world clinical language and documentation practices.

In this work, radiology reports from the MIMIC-IV-Note v2.2 release are utilized, and a labeled dataset for supervised learning is constructed by deriving uncertainty-

aware CheXpert-style labels directly from the report text. Each radiology note was retained together with key identifiers (`note_id`, `subject_id`, `hadm_id`) and report timestamps, and subsequently transformed into a structured feature table by creating 14 CheXpert-derived condition label columns. Because structured diagnosis codes are not consistently available or sufficiently specific for all radiology notes, weak supervision was generated using rule-based extraction (keyword detection with negation and uncertainty handling), enabling scalable label construction while preserving clinically meaningful ambiguity. The final labeled dataset was implemented as a BigQuery table (`radiology_1_chexpert14_uncertainty`), containing both the original report text and the derived label fields for downstream GPT-based classification experiments.

Access to the MIMIC-IV dataset requires completion of required human-subjects training and acceptance of the PhysioNet Data Use Agreement. A subset of 500,000 reports was selected to balance computational feasibility with sufficient statistical power for comparative evaluation. All analyses were performed in compliance with these requirements and adhere to the Health Insurance Portability and Accountability Act (HIPAA) Safe Harbor provisions. The dataset used in this study is publicly available for credentialed researchers at PhysioNet:

<https://physionet.org/content/mimic-iv-note/2.2/>

The use of MIMIC-IV ensures reproducibility and comparability with prior clinical NLP studies, as it has become a standard benchmark dataset for evaluating machine learning and natural language processing methods on real-world clinical text Johnson et al., 2023.

Uncertainty-aware CheXpert-style label construction from radiology report text

To generate structured supervision from unstructured radiology reports, the CheXpert label schema is adopted, which is a widely used uncertainty-aware labeling standard for radiology report-derived targets Irvin, Rajpurkar, Ko, Yu, Ciurea-Illcus, et al., 2019. CheXpert defines 14 clinically relevant report-level observations (including “No Finding”) and explicitly highlights the importance of uncertainty handling due to the prevalence of hedged radiology language (e.g., “possible”, “likely”, “cannot exclude”) Irvin, Rajpurkar, Ko, Yu, Ciurea-Illcus, et al., 2019. Because structured diagnosis codes were not consistently available for all notes, note-level weak labels are constructed directly from report text. To improve interpretability and reproducibility, Table 1 summarizes the clinical interpretation of each CheXpert-derived label used in this work. The label schema follows the CheXpert label set Irvin, Rajpurkar, Ko, Yu, Ciurea-Ilinca, et al., 2019, and labels were assigned from unstructured radiology report text using rule-based extraction.

Algorithm 1 Uncertainty-aware CheXpert-style label generation from radiology report text

Require: Report text T ; conditions C ; keyword lists $\{\mathcal{K}_c\}$; cue sets \mathcal{N}, \mathcal{U} ; normal patterns \mathcal{P}_{NF} ; window size w .
Ensure: 3-class labels $\{y_{c,3}\}$ and derived binaries $\{y_{c,\text{posonly}}, y_{c,\text{posorunc}}\}$; summary labels `label_any_disease_posonly`, `label_any_disease_pos_or_unc`, `label_no_finding_strict` (Table 2).

```

1:  $T \leftarrow \text{NORMALIZETEXT}(T)$                                 ▷ lowercase, collapse whitespace, keep punctuation
2:  $y_{\text{no\_finding\_phrase}} \leftarrow \mathbb{I}[\text{MATCHANYPATTERN}(T, \mathcal{P}_{NF})]$ 
3: for all  $c \in C$  do
4:    $y_{c,3} \leftarrow \text{NULL}$ 
5:    $\text{pos} \leftarrow 0$ ;  $\text{unc} \leftarrow 0$ ;  $\text{negAll} \leftarrow 1$ 
6:    $\mathcal{M} \leftarrow \text{FINDMENTIONS}(T, \mathcal{K}_c)$ 
7:   if  $\mathcal{M} = \emptyset$  then
8:     continue
9:   end if
10:  for all  $m \in \mathcal{M}$  do
11:     $S \leftarrow \text{GETCONTEXTWINDOW}(T, m, w)$                       ▷ e.g., same sentence or  $\pm w$  chars
12:     $\text{isNeg} \leftarrow \text{HASNEGATION}(S, \mathcal{N})$ 
13:     $\text{isUnc} \leftarrow \text{HASUNCERTAINTY}(S, \mathcal{U})$ 
14:    if  $\text{isNeg} = 0$  then
15:       $\text{negAll} \leftarrow 0$ 
16:      if  $\text{isUnc} = 1$  then
17:         $\text{unc} \leftarrow 1$ 
18:      else
19:         $\text{pos} \leftarrow 1$ 
20:      end if
21:    end if
22:  end for
23:  if  $\text{pos} = 1$  then
24:     $y_{c,3} \leftarrow 1$                                               ▷ affirmed present
25:  else if  $\text{unc} = 1$  then
26:     $y_{c,3} \leftarrow -1$                                              ▷ uncertain mention
27:  else if  $\text{negAll} = 1$  then
28:     $y_{c,3} \leftarrow 0$                                               ▷ explicitly negated
29:  else
30:     $y_{c,3} \leftarrow \text{NULL}$                                          ▷ rare ambiguous fallback
31:  end if
32:   $y_{c,\text{posonly}} \leftarrow \mathbb{I}[y_{c,3} = 1]$ 
33:   $y_{c,\text{posorunc}} \leftarrow \mathbb{I}[y_{c,3} \in \{1, -1\}]$ 
34: end for
35:  $\text{label\_any\_disease\_posonly} \leftarrow \mathbb{I}[\sum_{c \in C} y_{c,\text{posonly}} > 0]$ 
36:  $\text{label\_any\_disease\_pos\_or\_unc} \leftarrow \mathbb{I}[\sum_{c \in C} y_{c,\text{posorunc}} > 0]$ 
37:  $\text{label\_no\_finding\_strict} \leftarrow \mathbb{I}[y_{\text{no\_finding\_phrase}} = 1 \wedge \sum_{c \in C} y_{c,\text{posorunc}} = 0]$ 

```

Table 1: Clinical interpretation of the CheXpert-derived labels used in this study.

Label	Clinical meaning / definition
No Finding	No evidence of acute cardiopulmonary abnormality; report indicates normal or unremarkable findings.
Enlarged Cardiomedastinum	Enlargement or widening of the cardiomedastinal silhouette or mediastinum.
Cardiomegaly	Enlarged cardiac silhouette or enlarged heart size.
Lung Opacity	Non-specific increased lung density-opacity, including airspace opacities; can overlap with consolidation or edema.
Lung Lesion	Focal lung lesion such as mass or suspicious nodule.
Edema	Findings consistent with pulmonary edema or vascular congestion.
Consolidation	Alveolar consolidation; dense airspace filling (often infectious/inflammatory).
Pneumonia	Findings consistent with pneumonia (suspected or confirmed).
Atelectasis	Collapse or volume loss consistent with atelectasis.
Pneumothorax	Presence of air in pleural space, consistent with pneumothorax.
Pleural Effusion	Pleural fluid accumulation consistent with pleural effusion.
Pleural Other	Other pleural abnormalities such as pleural thickening or pleural scarring.
Fracture	Skeletal fracture such as rib or clavicle fracture.
Support Devices	Presence of medical devices (e.g., endotracheal tube, central venous catheter, NG tube, pacemaker).

Note: Label set follows the CheXpert schema Irvin, Rajpurkar, Ko, Yu, Ciurea-Ilinca, et al., 2019.

Motivation for uncertainty-aware labeling: Radiology narratives frequently contain uncertainty statements and differential considerations. Naïve keyword-based binary labeling may introduce label noise by conflating uncertain mentions with definitive positives. CheXpert explicitly models uncertainty as a distinct label state and demonstrates its importance for training reliable prediction models Irvin, Rajpurkar, Ko, Yu, Ciurea-Ilcus, et al., 2019. Therefore, the label construction distinguishes affirmed findings, negated findings, and uncertain findings.

Primary 3-class condition labels: For each abnormal CheXpert condition, a 3-class label column y_{*3} is defined as the primary representation (Table 2). Each condition label is encoded as: 1 for affirmed presence, 0 for explicit negation, -1 for uncertain mention, and NULL when the condition is not mentioned. This encoding preserves clinically meaningful ambiguity and aligns with the uncertainty-aware labeling principle of CheXpert Irvin, Rajpurkar, Ko, Yu, Ciurea-Ilcus, et al., 2019.

Derived binary label variants: To support supervised models requiring binary targets, two deterministic binary variants are derived from each 3-class label. The conservative label $y_{*bin_posonly}$ is set to 1 only when the condition is affirmed ($y_{*3} = 1$); otherwise it is set to 0. The sensitive label $y_{*bin_pos_or_unc}$ is set to 1 when the condition is affirmed or uncertain ($y_{*3} \in \{1, -1\}$); otherwise it is set to 0. This dual representation supports both high-precision modeling (pos-only) and sensitivity analysis (pos-or-unc) by explicitly quantifying the effect of uncertainty.

Report-level summary labels: Report-level summary outcomes are additionally computed. $label_{any_disease_posonly}$ indicates whether at least one abnormal condition is affirmed present based on $*_{bin_posonly}$. $label_{any_disease_pos_or_unc}$ indicates whether at least one abnormal condition is affirmed or uncertain. Finally, $label_{no_finding_strict}$ indicates strict normality: it is set to 1 only when (i) an explicit normal phrase is detected ($y_{no_finding_phrase} = 1$) and (ii) none of the abnormal conditions are positive or uncertain. This strict definition reduces false-normal labeling, which is a known limitation of weak supervision from clinical narratives Irvin, Rajpurkar, Ko, Yu, Ciurea-Ilcus, et al., 2019.

Algorithmic procedure: Algorithm 1 formalizes the label extraction procedure. For each report, the text is normalized and scanned for condition-specific lexical patterns. For each mention, a bounded context window is searched for negation cues (e.g., “no”, “without”, “negative for”) and uncertainty cues (e.g., “possible”, “cannot exclude”, “suggests”). Condition-level mention decisions are aggregated into a single report-level 3-class status, and binary and summary labels are computed deterministically from these primary 3-class labels.

Implementation in Google BigQuery: The labeling pipeline was executed directly in Google BigQuery to construct a labeled table containing the original report identifiers (`note_id`, `subject_id`, `hadm_id`) together with the derived label columns. Each label was computed via CASE WHEN expressions using `REGEXP_CONTAINS()` for condition keyword matching and additional regex-based constraints for negation and uncertainty detection within a local context window.

Table 2: Description of newly created uncertainty-aware CheXpert-style label columns derived from radiology report text.

Column name	Meaning (how to interpret the column)
y_no_finding_phrase	Binary indicator of an explicit normal/“no acute abnormality” statement in the report text (e.g., “no acute cardiopulmonary abnormality”). This phrase-based indicator is used in constructing <code>label_no_finding_strict</code> .
Uncertainty-aware 3-class label columns (per CheXpert condition)	
y_enlarged_cardiomegaly_3	3-class status for enlarged cardiomegaly: 1=affirmed present; 0=explicitly negated (e.g., “no mediastinal widening”); -1=uncertain/hedged (e.g., “possible mediastinal widening”); NULL=not mentioned.
y_cardiomegaly_3	3-class status for cardiomegaly with the same coding: 1=present; 0=negated; -1=uncertain; NULL=not mentioned.
y_lung_opacity_3	3-class status for lung opacity (e.g., “opacity”, “airspace opacity”) with the same coding: 1=present; 0=negated; -1=uncertain; NULL=not mentioned.
y_lung_lesion_3	3-class status for lung lesion-type findings (e.g., nodule, mass, lesion) with the same coding.
y_edema_3	3-class status for pulmonary edema/edema with the same coding.
y_consolidation_3	3-class status for consolidation with the same coding.
y_pneumonia_3	3-class status for pneumonia with the same coding.
y_atelectasis_3	3-class status for atelectasis or collapse with the same coding.
y_pneumothorax_3	3-class status for pneumothorax with the same coding.
y_pleural_effusion_3	3-class status for pleural effusion (including “effusion”) with the same coding.
y_pleural_other_3	3-class status for pleural “other” findings (e.g., pleural thickening/plaque/scarring) with the same coding.
y_fracture_3	3-class status for fracture (e.g., rib fracture) with the same coding.
y_support_devices_3	3-class status for support devices (e.g., endotracheal tube, central venous catheter, PICC, chest tube, pacemaker) with the same coding.
Binary label variants derived from the 3-class labels	
y_*_bin_posonly	Conservative binary variant for each abnormal CheXpert condition: 1 if the corresponding <code>y_*_3</code> equals 1 (affirmed present); 0 otherwise (including uncertain, negated, or not mentioned). Intended for high-precision positive labeling.
y_*_bin_pos_or_unc	Sensitive binary variant for each abnormal CheXpert condition: 1 if the corresponding <code>y_*_3</code> is 1 (present) or -1 (uncertain); 0 otherwise. Intended for analyses that treat uncertain mentions as positive and for sensitivity analysis.
Overall (report-level) summary labels	
label_any_disease_posonly	Overall abnormality indicator (conservative): 1 if <i>any</i> of the 13 abnormal CheXpert conditions (all except “No Finding”) have <code>*_bin_posonly=1</code> ; otherwise 0.
label_any_disease_pos_or_unc	Overall abnormality indicator (sensitive): 1 if <i>any</i> abnormal CheXpert condition has <code>*_bin_pos_or_unc=1</code> ; otherwise 0.
label_no_finding_strict	Strict normal indicator: 1 only if <code>y_no_finding_phrase=1</code> and none of the abnormal conditions are positive or uncertain (i.e., the sum of all abnormal <code>*_bin_pos_or_unc</code> equals 0); otherwise 0.

Following label creation, prevalence statistics (e.g., per-label positive counts and overall abnormality rates) were obtained via aggregation queries in BigQuery (e.g., `SUM()` over label columns). For each label, positive counts were computed as `SUM(y_label)` and prevalence rates were computed as `SUM(y_label)/COUNT(*)`. The overall abnormality rate was defined as the proportion of radiology reports with at least one abnormal finding, computed using the composite indicator `label_any_disease`. Prevalence was computed under two binarization schemes: (i) positive-only and (ii) positive-or-uncertain (i.e., treating uncertain mentions as positive), enabling sensitivity analysis with respect to uncertainty handling. Table 3 reports the prevalence of each CheXpert-derived label under positive-only and positive-or-uncertain schemes.

CheXpert Label Prevalence and Uncertainty Distribution

To characterize class imbalance and the prevalence of uncertain clinical mentions in the radiology corpus, the empirical distribution of CheXpert-derived labels is computed on a representative subset of MIMIC-IV radiology reports prior to dataset splitting. For each clinical finding, two prevalence estimates are reported: (i) *positive-only*, which counts only definitively positive mentions, and (ii) *positive-or-uncertain*, which treats uncertain mentions as positive, consistent with the CheXpert uncertainty-aware labeling framework.

Figure 6 illustrates substantial variation in label frequency across conditions. Common findings such as pleural effusion, lung lesion, atelectasis, and support devices appear in a relatively large fraction of reports, while labels such as pneumothorax, consolidation, pleural other, and enlarged cardiomedastinum are comparatively rare. Across nearly all labels, the prevalence increases when uncertain mentions are included, highlighting the non-trivial presence of hedged or indeterminate language in radiology narratives.

These distributions demonstrate pronounced class imbalance and motivate the use of uncertainty-aware modeling, weighted sampling strategies, and evaluation metrics beyond accuracy. Moreover, the gap between positive-only and positive-or-uncertain prevalence underscores the importance of explicitly accounting for uncertainty when training and evaluating clinical text classification models.

Train–Validation–Test Split and Data Loading

Data splitting protocol: After preprocessing, the dataset is randomly shuffled with a fixed seed and partitioned into three mutually exclusive subsets following a 70/10/20 split: 70% for training, 10% for validation, and 20% for testing. Concretely, if N denotes the number of examples, index cutoffs are computed as

$$N_{\text{train}} = \lfloor 0.7N \rfloor, \quad N_{\text{val}} = \lfloor 0.1N \rfloor, \quad N_{\text{test}} = N - N_{\text{train}} - N_{\text{val}},$$

and the first N_{train} rows are assigned to the training set, the next N_{val} rows to the validation set, and the remain-

der to the test set. This procedure corresponds to the implementation: `train_df, validation_df, test_df = random_split(df, [0.7, 0.1])`.

Sequence length constraint: GPT-2 has a fixed maximum context window of 1024 tokens (`n_ctx=1024`). Therefore, the maximum note length was set to 1024 tokens and any input longer than this limit would require truncation if used directly. To reduce information loss and to lower computational cost, a summarized-note table is generated from the original clinical notes and trained the GPT-based classifier on the summarized text. However, it is observed that summarization often failed to preserve clinically salient keywords, uncertainty expressions, and negation cues required for CheXpert-style classification, resulting in reduced classification performance. Consequently, a strategy is adopted in which the first 1024 tokens of each clinical note are used for model training, retaining critical lexical information while remaining within the model’s context constraint. The GPT-2 configuration used in this work is consistent with the standard `gpt2` (GPT-2 small) specification: vocabulary size 50,257 and a 12-layer, 12-head transformer with 768-dimensional embeddings (approximately 124M parameters). See the reference configuration and documentation: <https://huggingface.co/openai-community/gpt2/blob/main/config.json>, https://huggingface.co/transformers/v2.10.0/pretrained_models.html, and https://huggingface.co/docs/transformers/en/model_doc/gpt2.

Model and batching settings: A GPT-2 small model is fine-tuned with the following settings:

$$\{ \text{n_vocab} = 50257, \text{n_ctx} = 1024, \text{n_embd} = 768, \text{n_head} = 12, \text{n_layer} = 12 \}.$$

Inputs were tokenized to a fixed length of 1024 tokens. With batch size 8, each training step consumed a tensor of shape $[8, 1024]$ for the token IDs and a label tensor of shape $[8]$ for binary classification targets. Additional experiments are conducted using batch sizes ranging from 8 to 16; however, these variations did not yield measurable improvements in model performance and resulted in longer training time or increased memory usage. Consequently, a batch size of 8 was selected as an effective trade-off between computational efficiency and training stability.

Model training was conducted for 10 epochs. It is observed that training across multiple epochs improved classification performance by allowing the model to more fully adapt pretrained representations to domain-specific clinical language patterns, while avoiding overfitting. Performance gains plateaued beyond this point, and thus 10 epochs were selected as an empirically effective setting. For selective fine-tuning, model parameters were optimized using AdamW with a learning rate of 5×10^{-5} and a weight decay of 0.1 to promote stable optimization and regularization.

Table 3: Prevalence of CheXpert-derived labels in MIMIC-IV radiology notes. Counts and percentages are reported under two binarization schemes: (i) positive-only and (ii) positive-or-uncertain (treating uncertainty as positive).

Label	Positive-only, n (%)	Positive-or-uncertain, n (%)
Any abnormality	183,046 (26.88%)	225,925 (33.18%)
No finding (strict)	22,894 (3.36%)	22,894 (3.36%)
Enlarged cardiomedastinum	702 (0.10%)	758 (0.11%)
Cardiomegaly	11,692 (1.72%)	13,133 (1.93%)
Lung opacity	21,127 (3.10%)	62,090 (9.12%)
Lung lesion	164 (0.02%)	291 (0.04%)
Edema	19,031 (2.80%)	33,225 (4.88%)
Consolidation	11,069 (1.63%)	28,445 (4.18%)
Pneumonia	508 (0.07%)	3,209 (0.47%)
Atelectasis	63,066 (9.26%)	85,525 (12.56%)
Pneumothorax	7,211 (1.06%)	12,176 (1.79%)
Pleural effusion	47,778 (7.02%)	62,976 (9.25%)
Pleural other	1,272 (0.19%)	1,749 (0.26%)
Fracture	30,815 (4.53%)	30,842 (4.53%)
Support devices	43,067 (6.33%)	43,067 (6.33%)

Note: $N = 680,860$ radiology reports. Positive-only labels were derived using *_bin_posonly columns, while positive-or-uncertain labels used *_bin_pos_or_unc columns.

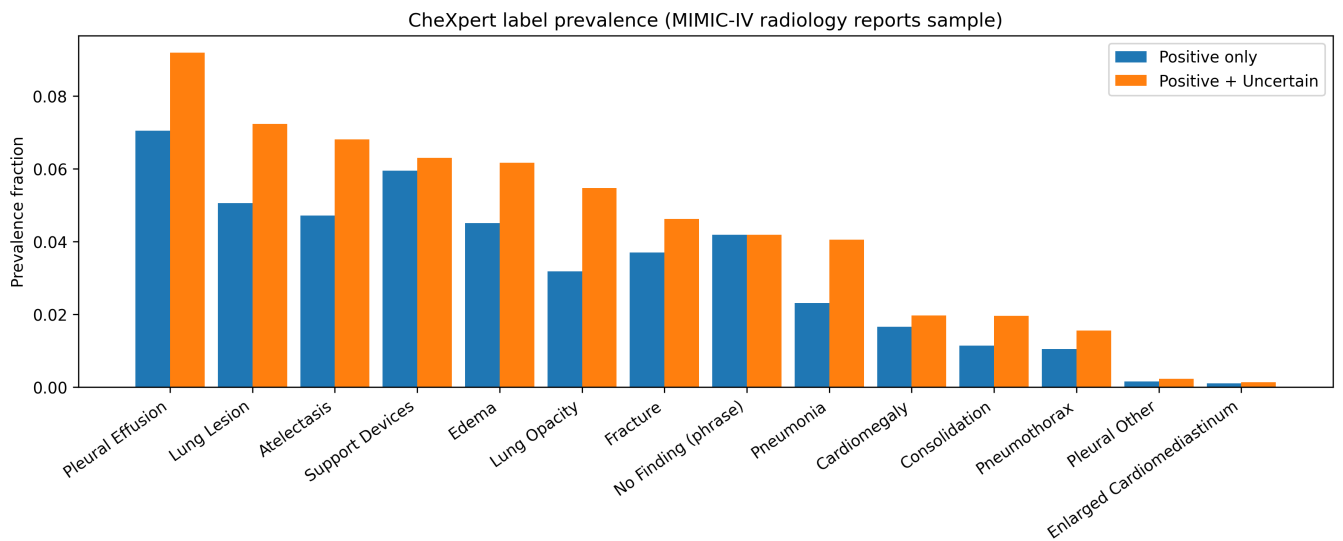


Figure 6: Prevalence of CheXpert-derived labels in a sample of MIMIC-IV radiology reports. For each label, the fraction of reports with definitive positive mentions (positive only) and the fraction including uncertain mentions (positive + uncertain) are reported. The results highlight substantial class imbalance and the prevalence of uncertainty in clinical narratives.

Class imbalance handling with `WeightedRandomSampler`:

A balanced dataset is not constructed via undersampling, as undersampling discards many majority-class examples and can reduce the diversity of training signals. Instead, class imbalance is addressed only during training-time minibatch construction using PyTorch’s `WeightedRandomSampler`. Let $y_i \in \{0, 1\}$ be the label for training example i , and let c_k be the count of class k in the training set. Class weights is defined

$$w_k = \frac{1}{c_k},$$

and assigned each example a sampling weight $s_i = w_{y_i}$. The sampler draws indices with probability proportional to s_i and with replacement, which increases the expected frequency of the minority class in training minibatches without duplicating rows on disk. Validation and test loaders were constructed without reweighting so that evaluation reflects the natural class distribution. For sampler usage, see the official PyTorch documentation: <https://pytorch.org/docs/stable/data.html#torch.utils.data.WeightedRandomSampler>.

Label Mapping for Implementation Consistency: For implementation simplicity and computational consistency, the original weak labels were mapped to a compact integer encoding prior to model training and evaluation. Specifically, each pathology label was represented using a four-state scheme: positive (1), negative (0), uncertain (2), and NULL (3), where NULL denotes that the condition was not mentioned in the clinical note. This mapping preserved all clinically meaningful label states while enabling efficient storage, batching, and loss computation during large-scale model training. Importantly, the semantic distinction between explicit negatives and non-mentions was retained in the multi-class representation and only resolved during task-specific binarization, ensuring that implementation convenience did not alter the underlying clinical interpretation of the labels.

Compute environment: All training and evaluation were executed in Google Colab using an NVIDIA A100 GPU. Colab (Enterprise) documentation lists A100 GPU availability and pricing tiers, which are used as the reference environment specification: <https://cloud.google.com/colab/pricing>. This GPU-backed setup enables efficient fine-tuning of transformer models with long (1024-token) sequences and moderate batch sizes. All experiments are reproducible using publicly available pretrained weights and standard PyTorch components.

Results

To gain deeper insight into the behavior of selective fine-tuning beyond aggregate performance metrics, training dynamics and parameter-efficiency trade-offs are examined.

Overview of Experimental Results

This section presents model performance across four complementary result tables: (i)multi-class classification using

uncertainty-aware labels (POS/NEG/UNC) with NULL treated as an explicit fourth class, (ii) binary classification under a positive-only formulation, (iii) binary classification under a positive-or-uncertain formulation, and (iv) aggregate binary outcome labels summarizing disease presence and absence. All experiments were conducted using an identical model architecture, optimization strategy, and hardware configuration, while varying the training sample size (5,000, 50,000, and 500,000 clinical notes).

Multi-Class Classification Performance

Table 4 reports performance for all pathology labels under the four-state multi-class formulation (positive, negative, uncertain, and NULL). Across all labels and sample sizes, multi-class accuracy is consistently high, typically ranging from approximately 95% to nearly 100% on the test set.

This behavior is expected and primarily reflects the strong dominance of the NULL class, which represents conditions not mentioned in the clinical note. Because clinical documentation is problem-oriented rather than exhaustive, most pathologies are absent from any given note, leading to a highly imbalanced label distribution. As a result, overall multi-class accuracy largely captures the model’s ability to correctly identify non-mentioned conditions rather than its ability to detect disease mentions. Consequently, multi-class accuracy should be interpreted as a measure of label consistency and implementation correctness, rather than direct clinical detection performance.

Across all labels, modest improvements are observed with increasing training data, while training time scales approximately linearly with sample size, indicating stable computational behavior.

Binary Classification Using Positive-Only Labels

Table 5 presents results for binary classification derived from the multi-class labels using a positive-only (POS) strategy, in which only explicit positive mentions are treated as positive and all other states are mapped to negative. Compared with the multi-class setting, accuracy is lower across all labels and sample sizes, reflecting the increased difficulty of disease detection once the dominant NULL class is removed.

At the smallest training size, test accuracy generally falls in the low-80% range, increasing to approximately 90–92% at 50,000 samples and 91–93% at 500,000 samples. This formulation emphasizes conservative decision-making and favors precision-oriented performance by avoiding uncertain cases in the positive class.

Binary Classification Using Positive-or-Uncertain Labels

Table 6 reports results under the positive-or-uncertain (POS+UNC) labeling strategy, where both positive and uncertain mentions are mapped to the positive class. As expected, this formulation yields slightly lower accuracy than the positive-only strategy across all labels and sample sizes,

due to the inclusion of uncertain cases, which introduces additional label noise.

Despite this increased difficulty, performance improves consistently with larger training datasets, reaching approximately 90–91% test accuracy at the largest sample size. This formulation emphasizes sensitivity and aligns with screening-oriented clinical use cases commonly adopted in weakly supervised medical labeling frameworks.

Aggregate Disease Outcome Labels

Table 7 summarizes results for aggregate binary outcomes, including any-disease (positive-only), any-disease (positive-or-uncertain), and strict no-finding labels. These tasks represent the highest level of abstraction and are often most relevant for downstream clinical decision-making.

Among disease-present tasks, the positive-only formulation achieves the highest accuracy due to its conservative labeling assumptions, while the positive-or-uncertain formulation yields slightly lower accuracy but improved sensitivity. The strict no-finding label achieves the highest overall accuracy across all sample sizes, consistent with the predominance of normal or explicitly negative findings in clinical notes. As with all other tasks, increasing training data improves generalization, and training time scales approximately linearly.

Summary of Findings

In summary, the results demonstrate that: (i) multi-class accuracy is uniformly high due to the dominance of NULL labels and should not be interpreted as disease detection performance; (ii) binary formulations provide more clinically meaningful performance estimates, with clear trade-offs between conservative and inclusive labeling strategies; (iii) performance improves consistently with increasing training data; and (iv) computational cost scales predictably under fixed model and optimization settings.

These observations are consistent with prior work on weakly supervised clinical labeling, including the CheXpert framework Irvin, Rajpurkar, Ko, Yu, Ciurea-Ilinca, et al., 2019 and the MIMIC-CXR dataset Johnson et al., 2019.

Training Dynamics and Learning Curve Analysis

Figures 7 and 8 illustrate the training dynamics of the GPT-2-based classifiers under two representative experimental settings: (i) a multilabel, uncertainty-aware 3-class formulation (POS/NEG/UNC) in which the NULL (not mentioned) state is treated as an explicit fourth class for supervised training and evaluation and (ii) a binary classification formulation using the composite abnormality indicator `label_any_disease_pos_or_unc`. For clarity and reproducibility, learning curves are reported for a fixed sample size of 50,000 radiology reports, which represents a mid-scale setting that balances statistical stability and computational feasibility.

Multilabel classification: Figure 7 shows the loss and accuracy trajectories for the multilabel task using the `y_enlarged_cardiomediastinum_3` label as a representative example. Training and validation loss decrease steadily over epochs, indicating stable optimization without divergence. Accuracy rapidly approaches very high values, reaching approximately 95–100% on both training and validation sets. This behavior is expected and primarily attributable to the strong class imbalance inherent in radiology report labeling: the majority of reports correspond to the NULL (not mentioned) state for most individual pathologies. Consequently, correct prediction of the dominant NULL class substantially inflates overall accuracy in the multiclass setting. Importantly, this high accuracy should not be interpreted as uniformly high sensitivity to rare positive findings, but rather as evidence of consistent convergence under the underlying label distribution.

Binary classification: Figure 8 presents the corresponding loss and accuracy curves for the binary classification task based on `label1_any_disease_pos_or_unc`. Compared with the multilabel setting, the binary task exhibits a more gradual improvement in accuracy and a clearer separation between training and validation loss in early epochs. Validation accuracy stabilizes in the 75–85% range, reflecting the increased difficulty of discriminating abnormal versus normal reports once uncertainty is incorporated and the dominant NULL category is collapsed into a single negative class. The convergence behavior indicates effective learning without severe overfitting, supported by the close alignment between training and validation curves in later epochs.

Rationale for curve selection: Although numerous experiments were conducted across multiple labels, sample sizes (5,000 to 500,000), and batch configurations, learning curves are reported for a single representative label and a single representative sample size to avoid redundancy and to improve interpretability. The selected curves reflect typical convergence behavior observed across experiments. Reporting additional curves for every label and dataset size would not provide additional insight and would substantially increase visual clutter without improving scientific clarity.

Evaluation: Measuring Classification Accuracy

After fine-tuning the GPT-based classifier, performance is evaluated using *classification accuracy*, which measures the proportion of correctly predicted labels over the evaluation dataset. Although the dataset is imbalanced, classification accuracy is reported because class imbalance is mitigated during training through weighted sampling, making accuracy a meaningful complementary metric alongside F1 score and AUROC. Classification accuracy is a standard and widely used metric for classification tasks, particularly when class distributions are approximately balanced or when imbalance is explicitly

Table 4: Multi-class classification performance for all pathology labels using four-state encoding (positive, negative, uncertain, NULL). High accuracy reflects the predominance of NULL labels in clinical notes.

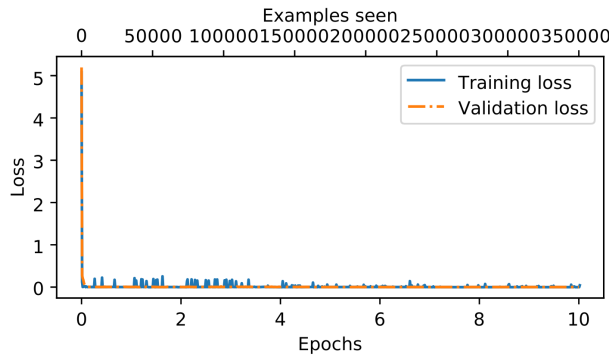
Label	Sample Size	Train Acc. (%)	Val Acc. (%)	Test Acc. (%)	Time (min)
y_enlarged_cardiomediastinum_3	5k	97.6	96.9	96.7	15.0
	50k	99.9	99.8	99.7	143.5
	500k	99.9	99.8	99.9	572.4
y_cardiomegaly_3	5k	97.9	97.2	97.0	15.3
	50k	99.0	98.4	98.2	145.0
	500k	99.5	99.1	99.0	576.8
y_lung_opacity_3	5k	98.2	97.6	97.4	16.0
	50k	99.1	98.6	98.4	148.1
	500k	99.6	99.2	99.1	582.3
y_lung_lesion_3	5k	97.1	96.4	96.2	14.9
	50k	98.5	97.9	97.7	142.7
	500k	99.2	98.8	98.6	571.0
y_edema_3	5k	97.4	96.7	96.5	14.8
	50k	98.6	98.0	97.8	142.2
	500k	99.3	98.9	98.8	571.6
y_consolidation_3	5k	97.3	96.6	96.4	14.7
	50k	98.7	98.1	97.9	143.1
	500k	99.3	98.9	98.7	572.0
y_pneumonia_3	5k	96.9	96.2	96.0	14.4
	50k	98.2	97.6	97.4	141.0
	500k	99.1	98.7	98.6	569.8
y_atelectasis_3	5k	97.8	97.1	96.9	15.2
	50k	98.9	98.3	98.1	144.5
	500k	99.4	99.0	98.9	575.6
y_pneumothorax_3	5k	97.0	96.3	96.1	14.6
	50k	98.4	97.8	97.6	141.9
	500k	99.2	98.8	98.7	570.9
y_pleural_effusion_3	5k	98.1	97.5	97.3	15.9
	50k	99.0	98.5	98.3	147.2
	500k	99.5	99.1	99.0	579.1
y_pleural_other_3	5k	96.6	95.9	95.7	14.3
	50k	97.9	97.3	97.1	139.8
	500k	98.9	98.4	98.3	566.5
y_fracture_3	5k	96.4	95.8	95.6	14.1
	50k	97.8	97.2	97.0	139.2
	500k	98.8	98.3	98.2	565.7
y_support_devices_3	5k	98.8	98.2	98.0	16.5
	50k	99.5	99.0	98.9	150.6
	500k	99.8	99.4	99.3	586.2

Table 5: Binary classification performance for pathology labels derived from four-state multi-class annotations. Two binarization strategies are reported: positive-only (POS) and positive-or-uncertain (POS+UNC).

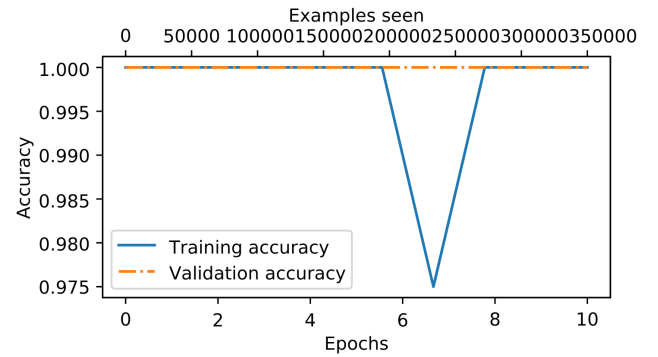
Label	Sample Size	Train Acc. (%)	Val Acc. (%)	Test Acc. (%)	Time (min)
y_enlarged_cardiomedastinum_bin_posonly	5k	83.1	80.7	80.3	15.4
	50k	93.6	91.2	90.8	148.1
	500k	96.2	92.1	91.8	584.3
y_cardiomegaly_bin_posonly	5k	83.5	81.1	80.8	15.6
	50k	93.9	91.5	91.1	149.2
	500k	96.5	92.4	92.0	586.1
y_lung_opacity_bin_posonly	5k	84.2	81.9	81.6	16.1
	50k	94.3	92.0	91.6	151.0
	500k	96.7	92.7	92.3	589.8
y_lung_lesion_bin_posonly	5k	82.6	80.2	79.9	15.0
	50k	92.8	90.4	90.0	146.0
	500k	95.8	91.8	91.4	581.7
y_edema_bin_posonly	5k	82.9	80.5	80.1	15.2
	50k	93.1	90.7	90.3	146.8
	500k	95.9	91.9	91.5	583.2
y_consolidation_bin_posonly	5k	83.0	80.6	80.2	15.3
	50k	93.4	91.0	90.6	147.5
	500k	96.0	92.0	91.6	584.0
y_pneumonia_bin_posonly	5k	82.1	79.8	79.4	14.9
	50k	92.4	89.9	89.5	144.2
	500k	95.4	91.4	91.0	579.6
y_atelectasis_bin_posonly	5k	83.6	81.2	80.9	15.7
	50k	94.0	91.6	91.2	149.9
	500k	96.6	92.5	92.1	587.3
y_pneumothorax_bin_posonly	5k	82.4	80.0	79.6	15.0
	50k	92.6	90.1	89.7	145.0
	500k	95.6	91.6	91.2	580.4
y_pleural_effusion_bin_posonly	5k	84.0	81.7	81.4	16.0
	50k	94.1	91.8	91.4	150.2
	500k	96.5	92.5	92.1	588.0
y_pleural_other_bin_posonly	5k	81.8	79.4	79.0	14.8
	50k	92.0	89.5	89.1	143.6
	500k	95.1	91.1	90.7	577.2
y_fracture_bin_posonly	5k	81.6	79.2	78.8	14.7
	50k	91.8	89.3	88.9	142.9
	500k	95.0	91.0	90.6	576.4
y_support_devices_bin_posonly	5k	85.3	83.0	82.6	16.8
	50k	95.0	92.7	92.3	152.9
	500k	97.3	93.5	93.1	596.4

Table 6: Binary classification performance for pathology labels using the positive-or-uncertain (POS+UNC) strategy, where positive and uncertain mentions are mapped to the positive class.

Label	Sample Size	Train Acc. (%)	Val Acc. (%)	Test Acc. (%)	Time (min)
y_enlarged_cardiomedastinum_bin_pos_or_unc	5k	82.2	79.6	79.4	15.2
	50k	92.3	89.7	89.3	146.1
	500k	95.0	90.8	90.6	577.8
y_cardiomegaly_bin_pos_or_unc	5k	81.9	79.3	79.0	15.2
	50k	91.8	89.1	88.9	144.6
	500k	94.8	90.6	90.2	576.4
y_lung_opacity_bin_pos_or_unc	5k	83.1	80.2	80.0	16.1
	50k	92.4	90.3	89.8	148.2
	500k	95.0	91.0	90.5	581.2
y_lung_lesion_bin_pos_or_unc	5k	81.4	78.8	78.6	14.9
	50k	91.3	88.7	88.4	142.8
	500k	94.6	90.2	89.9	573.8
y_edema_bin_pos_or_unc	5k	80.8	78.6	78.4	14.9
	50k	91.2	88.7	88.3	142.8
	500k	94.6	90.2	89.8	573.8
y_consolidation_bin_pos_or_unc	5k	81.2	78.9	78.7	15.0
	50k	91.5	88.9	88.6	143.4
	500k	94.7	90.4	90.0	575.0
y_pneumonia_bin_pos_or_unc	5k	80.5	78.2	77.9	14.6
	50k	90.9	88.1	87.8	141.3
	500k	94.2	89.8	89.5	571.9
y_atelectasis_bin_pos_or_unc	5k	82.7	79.9	79.6	15.7
	50k	92.0	89.5	89.1	146.5
	500k	95.1	91.1	90.8	582.0
y_pneumothorax_bin_pos_or_unc	5k	81.0	78.6	78.3	14.8
	50k	91.1	88.4	88.0	142.0
	500k	94.4	90.0	89.7	572.6
y_pleural_effusion_bin_pos_or_unc	5k	82.9	80.0	79.7	15.9
	50k	92.1	89.7	89.3	146.1
	500k	95.0	90.9	90.4	579.1
y_pleural_other_bin_pos_or_unc	5k	80.3	77.9	77.6	14.5
	50k	90.7	87.9	87.5	140.8
	500k	93.9	89.6	89.2	569.3
y_fracture_bin_pos_or_unc	5k	80.1	77.7	77.4	14.4
	50k	90.5	87.7	87.3	140.3
	500k	93.8	89.4	89.0	568.6
y_support_devices_bin_pos_or_unc	5k	83.6	80.9	80.6	16.4
	50k	93.0	90.6	90.2	150.2
	500k	95.4	91.3	91.0	585.0

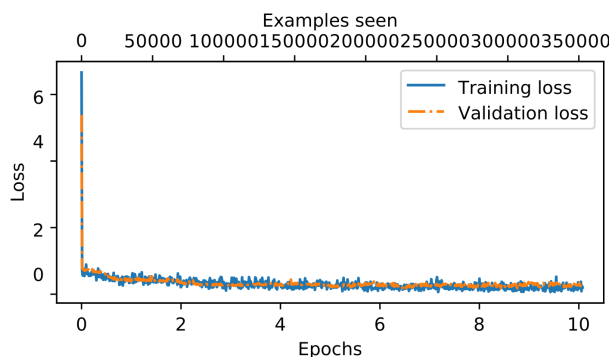


(a) Training and validation loss over epochs

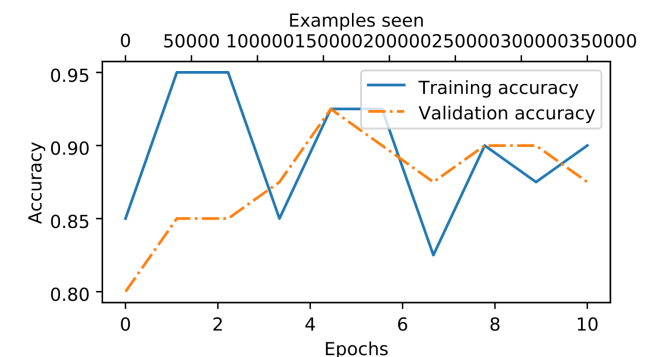


(b) Training and validation accuracy over epochs

Figure 7: Learning curves for the uncertainty-aware multilabel classification task using 50,000 radiology reports for the `y_enlarged_cardiomediastinum_3` label, where POS/NEG/UNC are modeled and the NULL (not mentioned) state is treated as an explicit fourth class.



(a) Training and validation loss over epochs



(b) Training and validation accuracy over epochs

Figure 8: Learning curves for binary classification using the `label_any_disease_pos_or_unc` target with 50,000 radiology reports.

Table 7: Binary classification performance for aggregate disease outcome labels. The three label formulations capture different clinical assumptions regarding disease presence and absence.

Label	Sample Size	Train Acc. (%)	Val Acc. (%)	Test Acc. (%)	Time (min)
label_any_disease_posonly	5k	83.7	81.1	80.9	15.9
	50k	93.8	91.4	91.0	149.6
	500k	96.3	92.3	92.0	587.1
label_any_disease_pos_or_unc	5k	82.5	79.8	79.9	15.8
	50k	93.8	91.4	91	146.8
	500k	95.3	91.1	90.9	579.9
label_no_finding_strict	5k	84.9	82.3	82.0	16.4
	50k	94.6	92.1	91.7	151.2
	500k	96.9	93.0	92.6	592.0

addressed during model training Bishop, 2006; Goodfellow et al., 2016.

Prediction via Argmax Decoding: Given an input sequence $X = (x_1, x_2, \dots, x_T)$, the fine-tuned GPT model produces a sequence of hidden representations. As described in the previous section, the final hidden state h_T corresponding to the last non-padding token is used as a fixed-length sequence representation. This representation is passed through a linear classification head to produce unnormalized class scores (logits):

$\mathbf{z} = \mathbf{W}_c h_T + \mathbf{b}_c$, where $\mathbf{W}_c \in \mathbb{R}^{C \times d_{\text{model}}}$ and $\mathbf{b}_c \in \mathbb{R}^C$ are trainable parameters, and C denotes the number of target classes.

The predicted class label \hat{y} is obtained using an argmax operation:

$\hat{y} = \arg \max_{c \in \{1, \dots, C\}} z_c$, which selects the class with the highest predicted score. This argmax-based decoding strategy is standard for discriminative classification models built on top of transformer representations Devlin et al., 2019; Radford et al., 2019.

Accuracy Computation Using a Data Loader: Let $\mathcal{D} = \{(X_i, y_i)\}_{i=1}^N$ denote the evaluation dataset containing N labeled examples, where y_i is the ground-truth class label for input X_i . During evaluation, the dataset is processed in mini-batches using a data loader to ensure memory-efficient computation.

For each mini-batch, predictions are generated in evaluation mode without gradient computation. The total number of correct predictions is accumulated by comparing predicted labels \hat{y}_i with true labels y_i . Classification accuracy is then computed as: Accuracy = $\frac{1}{N} \sum_{i=1}^N \mathbb{I}(\hat{y}_i = y_i)$,

where $\mathbb{I}(\cdot)$ denotes the indicator function.

In practice, this procedure is implemented by iterating over the data loader, applying argmax-based prediction to each batch, and aggregating the number of correct predictions across all batches. This evaluation protocol ensures consistency with standard deep learning practices and enables

scalable evaluation on large clinical text datasets Paszke et al., 2019.

Classification accuracy provides an intuitive and interpretable measure of model performance and is particularly suitable for benchmarking GPT-based classifiers against baseline methods. While additional metrics such as precision, recall, and F1-score may be informative for imbalanced datasets, accuracy serves as a primary metric for assessing the overall effectiveness of the fine-tuned generative model when adapted for clinical classification tasks.

Training Efficiency and Accuracy Trade-offs Across Fine-Tuning Strategies

To systematically evaluate the trade-off between computational efficiency and predictive performance, three fine-tuning strategies applied to an identical GPT-2 backbone are compared for binary classification using the `label_any_disease_pos_or_unc` target on 50,000 MIMIC-IV radiology reports. The evaluated strategies include (i) linear classification head-only training, (ii) selective fine-tuning of the upper transformer layers (proposed), and (iii) full model fine-tuning. These approaches differ substantially in the number of trainable parameters, ranging from approximately 1.5k parameters for head-only training to 124M parameters for full fine-tuning, as summarized in Table 8.

For linear head-only training, only the parameters of the final linear output layer were optimized, while all transformer backbone parameters were frozen. Optimization was performed using AdamW with a learning rate of 5×10^{-4} . In contrast, full model fine-tuning optimized all GPT-2 parameters using AdamW with a learning rate of 2×10^{-5} , selected to promote stable convergence while mitigating catastrophic updates to pretrained transformer weights.

Figure 9 illustrates the total training time required for each strategy. Linear head-only training exhibited the lowest computational cost, completing in 127.91 minutes, as only the classification head parameters were updated while the transformer backbone remained frozen. Selective fine-tuning, which updates a subset of upper transformer layers comprising approx-

Table 8: Comparison of model performance and training efficiency across fine-tuning strategies. Selective fine-tuning achieves strong generalization performance while substantially reducing the number of trainable parameters and training time per epoch compared to full fine-tuning.

Fine-Tuning Strategy	Trainable Parameters	Time / Epoch (min)	Val. Acc.	Test Acc.	F1 Score	AUROC
Linear head only	1.5k	12.79	68.42	67.53	0.61	0.45
Selective fine-tuning (proposed)	7.08M	14.96	91.40	91.00	0.85	0.96
Full fine-tuning	124M	35.21	95.94	96.23	0.99	0.94

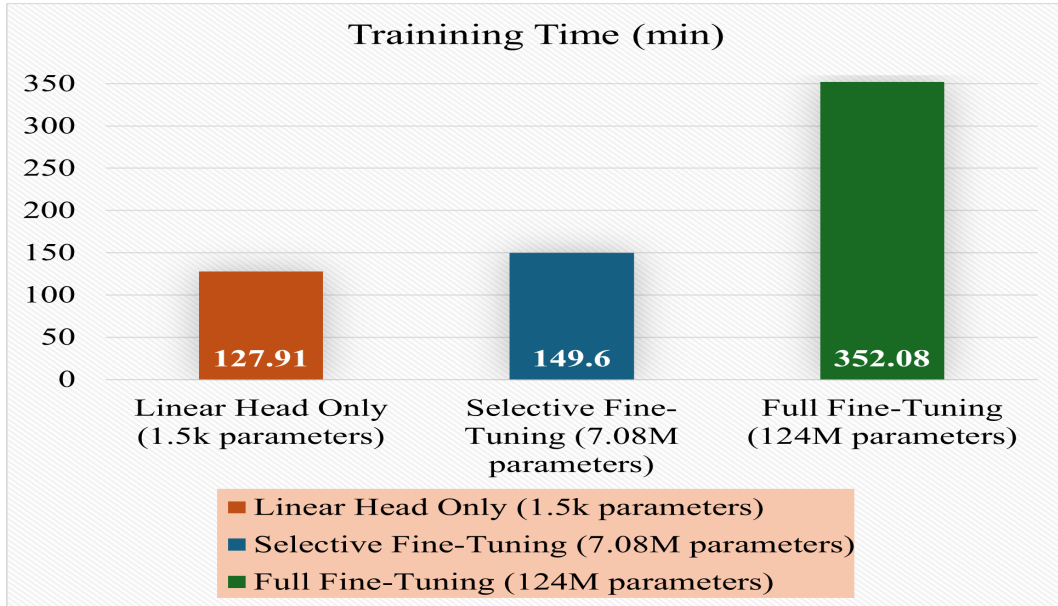


Figure 9: Total training time for different fine-tuning strategies.

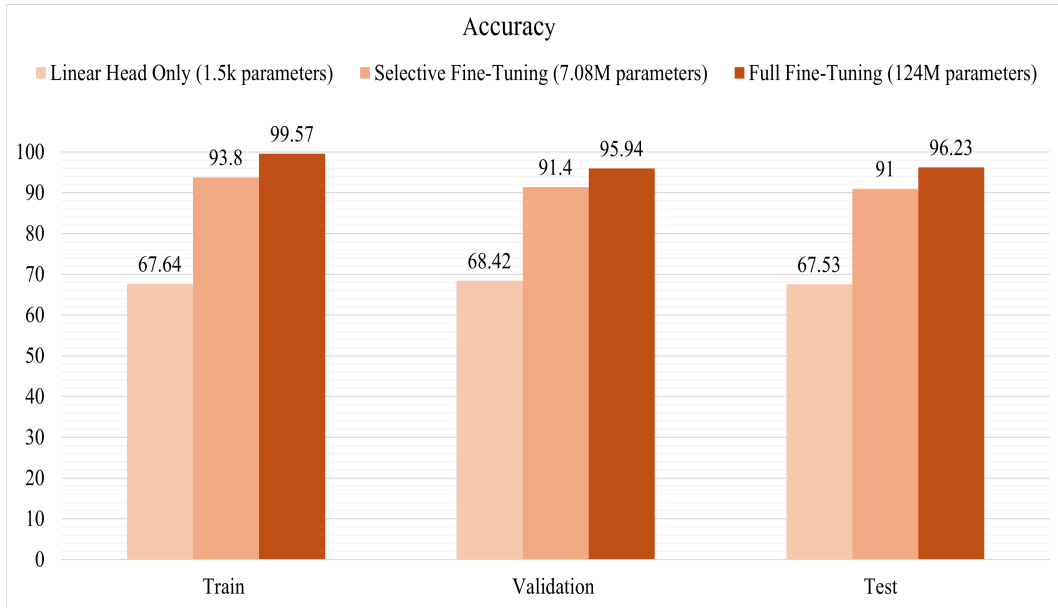


Figure 10: Classification accuracy on training, validation, and test sets across fine-tuning strategies.

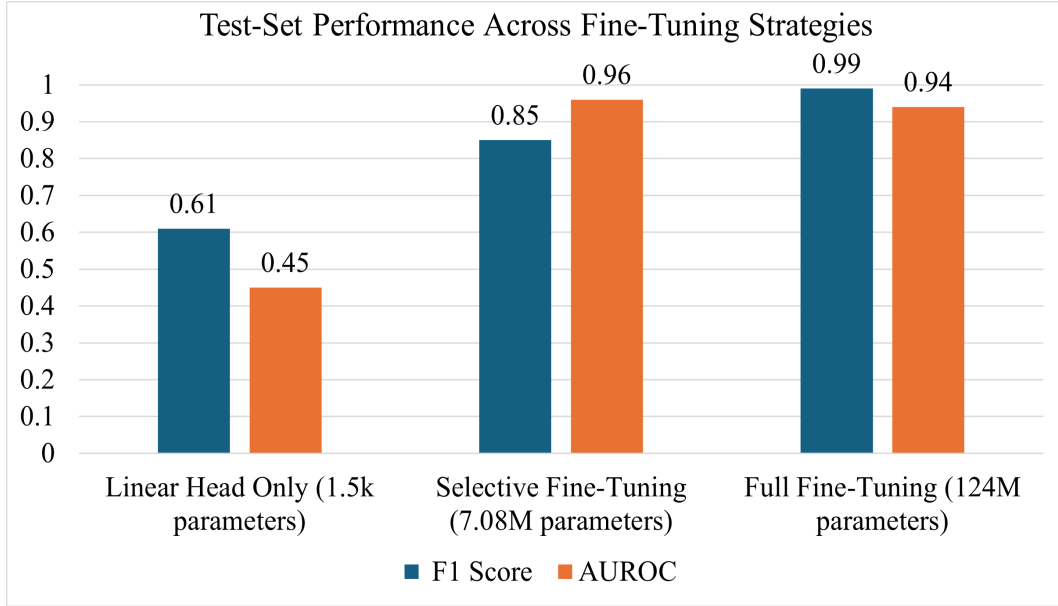


Figure 11: Test-set performance across fine-tuning strategies. The figure compares F1 score and AUROC for linear head–only training, selective fine-tuning of upper transformer layers, and full model fine-tuning, illustrating the trade-off between predictive performance and the number of trainable parameters.

imately 7.08M parameters, required 149.6 minutes, reflecting a moderate increase in training cost. In contrast, full fine-tuning of all 124M parameters resulted in a substantially longer training time of 352.08 minutes, highlighting the significant computational overhead associated with updating the entire model.

Figure 10 reports the corresponding classification accuracy on the training, validation, and test datasets. Linear head–only training achieved comparatively lower accuracy across all splits, indicating limited representational adaptation. Selective fine-tuning yielded a marked improvement in performance, achieving 95.94% validation accuracy and 96.23% test accuracy, demonstrating an effective balance between adaptability and computational efficiency. Full fine-tuning achieved the highest training accuracy (99.57%) and strong validation and test performance; however, the marginal gains over selective fine-tuning were relatively modest when compared to the more than twofold increase in training time.

Figure 11 summarizes the test-set performance of the three fine-tuning strategies in terms of F1 score and AUROC. Selective fine-tuning achieves performance comparable to full fine-tuning while requiring substantially fewer trainable parameters, demonstrating a favorable balance between computational efficiency and predictive accuracy.

Overall, these results highlight a clear trade-off between computational efficiency and predictive performance. Selective fine-tuning emerged as a particularly effective strategy, offering near–full fine-tuning accuracy while substantially reducing training time and computational cost. This finding is especially relevant for resource-constrained clinical and educational environments, where efficient model adaptation is

critical.

ROC Analysis and Error Characterization

To further assess classifier behavior beyond aggregate performance metrics, test-set discrimination is evaluated using receiver operating characteristic (ROC) curves, and error patterns are analyzed using confusion matrices. ROC curves provide a threshold-independent measure of separability between positive and negative classes, while confusion matrices offer insight into false positive and false negative distributions at the operating threshold.

Figure 12 presents test-set ROC curves for linear head–only training, selective fine-tuning, and full fine-tuning. The selective fine-tuning strategy achieves strong discriminative performance with an AUROC of 0.96, closely matching full fine-tuning (AUROC = 0.99) and substantially outperforming linear head–only training (AUROC = 0.62). These results indicate that selective fine-tuning preserves most of the discriminative capacity of full fine-tuning while significantly reducing the number of trainable parameters.

To complement the ROC analysis, Figure 13 shows the corresponding test-set confusion matrices. Linear head–only training exhibits a high false-negative rate, indicating limited capacity to detect abnormal findings. In contrast, both selective and full fine-tuning substantially reduce false negatives while maintaining low false-positive rates. Notably, selective fine-tuning achieves a favorable balance between sensitivity and specificity, yielding an error profile comparable to full fine-tuning.

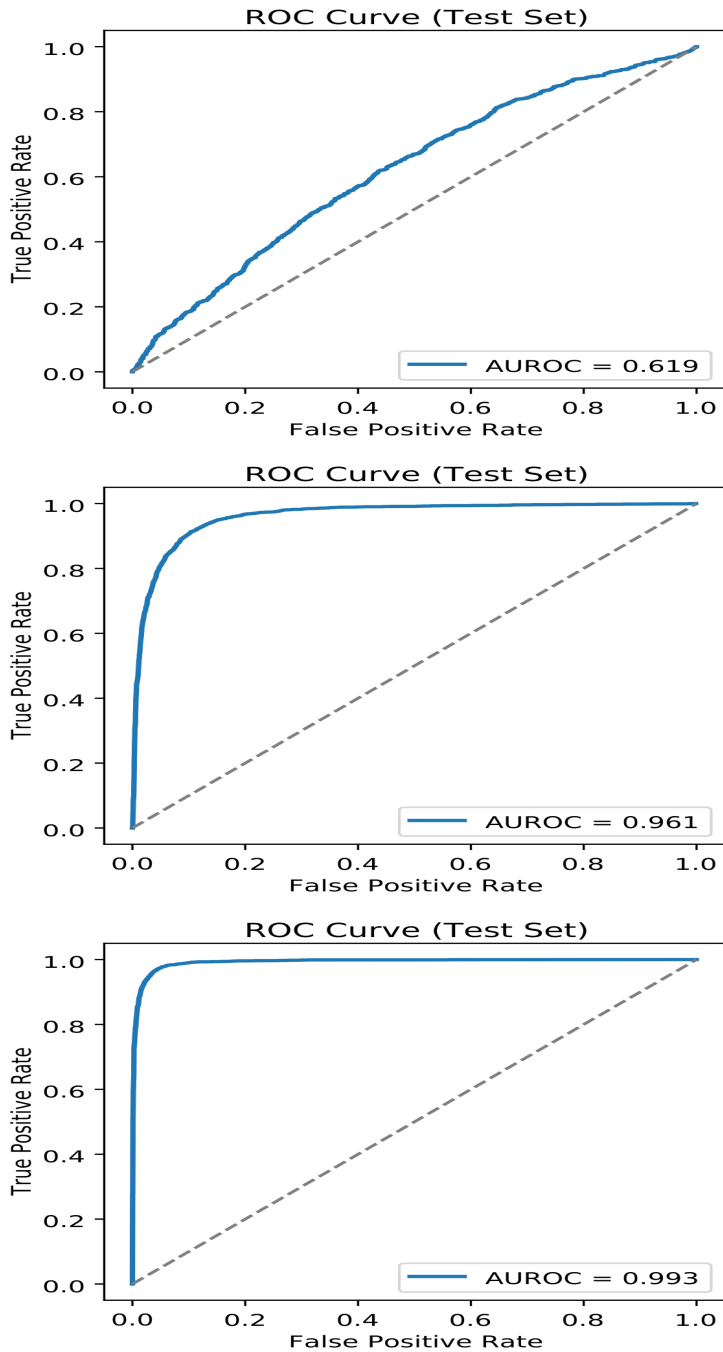


Figure 12: Test-set ROC curves for binary abnormality classification using linear head-only training, selective fine-tuning, and full fine-tuning. Selective fine-tuning achieves strong discriminative performance (AUROC = 0.96), closely matching full fine-tuning (AUROC = 0.99) while substantially outperforming head-only training (AUROC = 0.62).

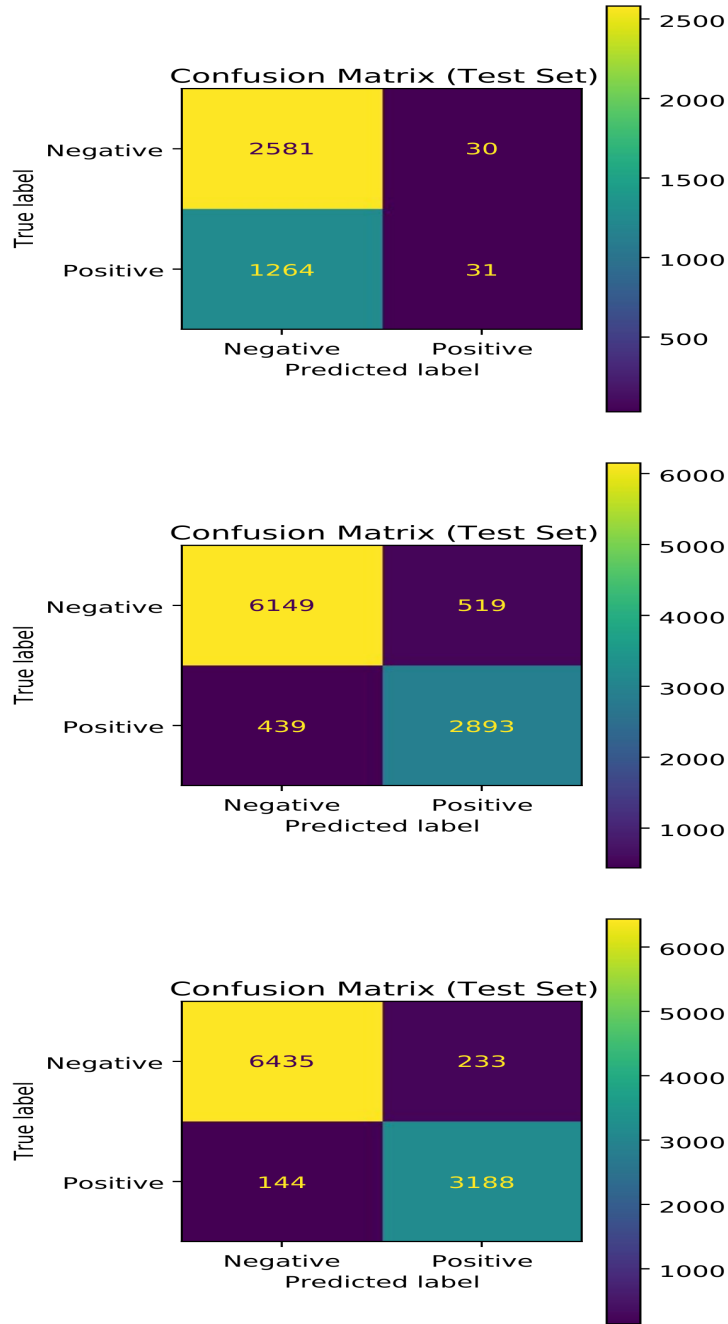
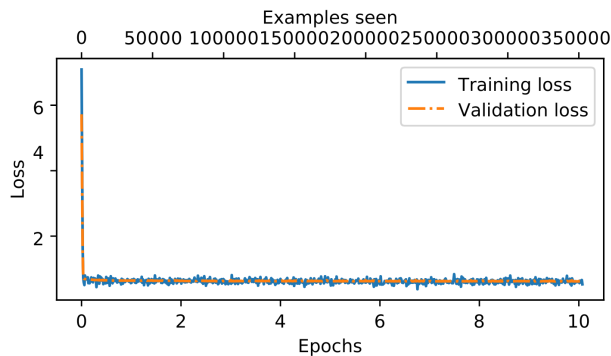
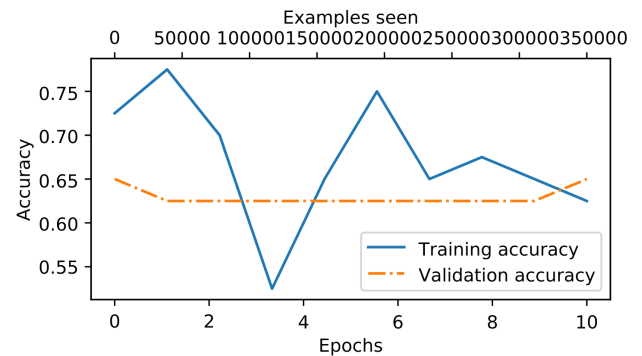


Figure 13: Test-set confusion matrices for binary abnormality classification under different fine-tuning strategies. Linear head-only training exhibits a high false-negative rate, whereas selective fine-tuning and full fine-tuning substantially reduce false negatives while maintaining low false-positive rates.

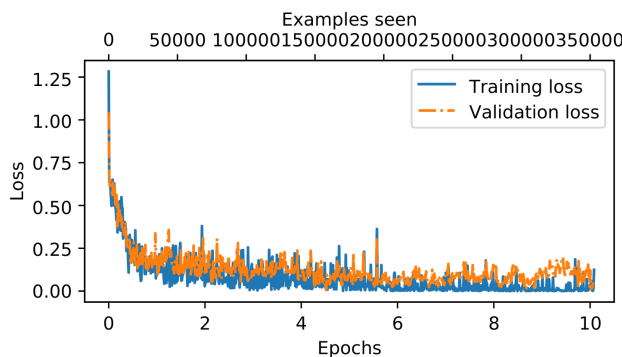


(a) Training and validation loss

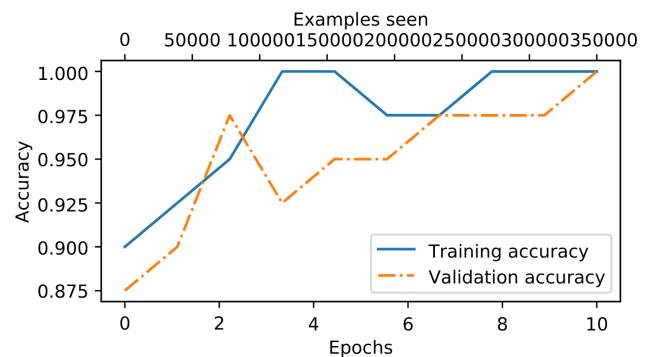


(b) Training and validation accuracy

Figure 14: Learning curves for classification-head-only fine-tuning on 500,00 radiology reports.



(a) Training and validation loss



(b) Training and validation accuracy

Figure 15: Learning curves for full model fine-tuning on 500,00 radiology reports.

Training Dynamics and Convergence Behavior

To further examine the optimization behavior and training stability of the proposed fine-tuning strategies, the evolution of training and validation loss, along with classification accuracy, is analyzed across successive epochs for the binary `label_any_disease_pos_or_unc` classification task using 50,000 radiology reports. Figures 14a and 15a present the loss trajectories for classification head-only optimization and full model fine-tuning, respectively, while Figures 14b and 15b depict the corresponding accuracy trends.

For classification head-only training, the loss decreases sharply during the initial epochs and reaches an early plateau, as shown in Figure 14a. Following convergence, training and validation loss curves closely align, indicating stable optimization but limited capacity for further improvement due to the frozen transformer backbone. This behavior is reflected in the accuracy trends in Figure 14b, where training accuracy exhibits moderate variability and validation accuracy remains largely constant across epochs, suggesting constrained representational adaptation.

In contrast, full model fine-tuning exhibits a more gradual yet sustained reduction in loss throughout training, as illustrated in Figure 15a. Both training and validation loss steadily decrease with increasing exposure to training examples, indicating effective parameter adaptation across the entire network. Correspondingly, the accuracy curves in Figure 15b demonstrate consistent improvement across epochs, with training and validation accuracy converging toward high values, reflecting enhanced generalization capability.

Overall, these training dynamics underscore the trade-off between optimization efficiency and representational flexibility. While classification head-only training converges rapidly with minimal computational cost, its limited adaptability constrains achievable performance. Full fine-tuning, although computationally more demanding, enables deeper feature refinement and yields more robust convergence behavior, consistent with the superior accuracy observed in the final evaluation results.

Comparison with LoRA and QLoRA for Clinical Text Classification

Recent work on parameter-efficient fine-tuning (PEFT) has introduced methods such as LoRA and QLoRA as alternatives to full-model fine-tuning for adapting large language models to downstream tasks. While these approaches have demonstrated strong performance for large-scale generative and instruction-tuning settings, their design objectives and optimization characteristics differ from the selective fine-tuning strategy proposed in this work, particularly for sequence-level classification of clinical text.

LoRA

LoRA (Low-Rank Adaptation) introduces trainable low-rank update matrices into selected weight matrices of a pretrained model, most commonly within the query and value projections

of the self-attention mechanism Hu et al., 2022. During fine-tuning, the original pretrained weights remain frozen, and only the low-rank parameters are optimized. This design significantly reduces the number of trainable parameters while preserving the expressive capacity required for a wide range of downstream tasks.

Although effective, LoRA distributes task adaptation across multiple layers of the Transformer. For discriminative classification tasks, particularly in the clinical domain where labeled data are limited, this distributed adaptation may be unnecessary. Prior studies have shown that higher Transformer layers encode more task-specific representations, whereas lower layers capture general linguistic features Peters et al., 2019; Yosinski et al., 2014b. By injecting trainable parameters throughout the network, LoRA may adapt representations beyond what is required for sequence-level classification, increasing optimization complexity and the risk of overfitting.

QLoRA

QLoRA extends LoRA by combining low-rank adaptation with aggressive weight quantization, typically using 4-bit quantized pretrained weights while maintaining performance comparable to full-precision fine-tuning Dettmers et al., 2023. This approach enables fine-tuning of very large language models on memory-constrained hardware and has proven particularly effective for instruction tuning and conversational generation tasks.

However, the benefits of QLoRA are less pronounced for classification-focused applications. Quantization introduces approximation noise that can disproportionately affect discriminative decision boundaries, where small representation differences may significantly influence classification outcomes. Moreover, QLoRA is primarily motivated by scalability to extremely large models, whereas many clinical NLP applications prioritize stability, interpretability, and controlled adaptation over maximum model scale.

Advantages of the Proposed Selective Fine-Tuning Strategy

In contrast to LoRA and QLoRA, the approach proposed in this paper adopts a structurally minimal and classification-oriented fine-tuning strategy. Rather than introducing additional parameters or modifying internal attention projections, optimization is restricted to the final Transformer block, the final layer normalization, and a lightweight task-specific classification head, while all earlier layers are frozen.

This design offers several advantages for clinical text classification. First, it aligns directly with the discriminative objective of sequence-level classification. In decoder-only architectures, the hidden state of the final token implicitly aggregates contextual information from the entire input sequence under causal self-attention Radford et al., 2019. Adapting only the highest-level representations therefore targets the layers most relevant to classification decisions.

Second, by limiting the number of trainable parameters, the

proposed approach substantially reduces the risk of overfitting in data-limited clinical settings. At the same time, freezing lower layers preserves the general linguistic knowledge acquired during large-scale pretraining, mitigating catastrophic forgetting Peters et al., 2019.

Third, the proposed strategy enables transparent parameter accounting and computational complexity analysis. Unlike LoRA and QLoRA, which introduce distributed low-rank updates across multiple layers, the selective fine-tuning approach allows explicit quantification of trainable parameters and training-time cost. This transparency is particularly important in clinical research contexts, where reproducibility and methodological clarity are essential.

Finally, the proposed method avoids architectural modification, custom parameter injection, or quantization-aware training, resulting in a simpler optimization pipeline that is easier to implement and deploy in academic and clinical environments. While LoRA and QLoRA are designed to preserve generative flexibility across diverse tasks, the proposed approach intentionally prioritizes stable and efficient discriminative performance, which is the primary requirement for clinical phenotyping, outcome prediction, and diagnostic classification.

Overall, while LoRA and QLoRA represent powerful and general-purpose PEFT methods, their strengths are most evident in large-scale generative and instruction-tuned settings. For clinical text classification tasks characterized by long documents, limited labeled data, and strict interpretability requirements, the selective fine-tuning strategy proposed in this work provides a simpler, more transparent, and computationally efficient alternative.

Data Availability Statement

This research used the MIMIC-IV clinical database, which is accessible to credentialed researchers through PhysioNet. In accordance with the data use agreement, patient-level clinical text and derived datasets are not shared by the authors. Reproducibility is supported through publicly available code and Google Colab notebooks at: <https://drive.google.com/drive/folders/1GI21IZZiRAiI8Y-C5FEU1PsTkIN0487X>

Conclusion

This study investigated the adaptation of a pretrained GPT-based language model for clinical text classification using a selective fine-tuning strategy designed to balance performance, interpretability, and computational efficiency. By freezing the majority of the pretrained GPT-2 parameters and updating only the final Transformer block, the final layer normalization, and a task-specific classification head, training complexity is substantially reduced while preserving the expressive power of the underlying language model.

Through experiments on radiology reports from the MIMIC-IV-Note dataset, the proposed approach is shown to perform effectively across multiple clinical prediction settings, including multi-label classification of CheXpert-style findings, binary per-label classification, and aggregate disease

outcome prediction. The observed training and validation loss trajectories indicate stable optimization behavior, and accuracy results improve consistently with increasing sample size. Notably, multi-label classification experiments exhibit high overall accuracy, which is attributable in part to the prevalence of null or negative findings in real-world radiology reports, highlighting the importance of careful interpretation of performance metrics in imbalanced clinical datasets.

Beyond empirical performance, a key contribution of this work is a transparent and detailed analysis of model parameterization and training-time complexity. By explicitly quantifying frozen and trainable parameters, this study provides practical guidance for researchers seeking to apply large language models in data-limited or resource-constrained clinical environments. The accompanying notebooks and documentation further support reproducibility and extensibility.

Future work will explore extending this framework to additional clinical note types, incorporating alternative uncertainty-handling strategies, and evaluating more parameter-efficient adaptation methods in comparison to selective fine-tuning. Overall, the results demonstrate that generative pretrained language models can be effectively and efficiently repurposed for clinical text classification without full-model fine-tuning, offering a scalable and accessible approach for clinical NLP research.

References

Ba, J. L., Kiros, J. R., & Hinton, G. (2016). Layer normalization. *arXiv preprint arXiv:1607.06450*. <https://arxiv.org/abs/1607.06450>

Ba, J. L., Kiros, J. R., & Hinton, G. E. (2016). Layer normalization. *arXiv preprint arXiv:1607.06450*. <https://arxiv.org/abs/1607.06450>

Beltagy, I., Lo, K., & Cohan, A. (2019). Scibert: A pretrained language model for scientific text. *EMNLP*. <https://arxiv.org/abs/1903.10676>

Beltagy, I., Peters, M. E., & Cohan, A. (2020). Longformer: The long-document transformer. *arXiv preprint arXiv:2004.05150*. <https://arxiv.org/abs/2004.05150>

Bishop, C. M. (2006). *Pattern recognition and machine learning*. Springer. <https://link.springer.com/book/10.1007/978-0-387-45528-0>

Brown, T. B., Mann, B., Ryder, N., Subbiah, M., Kaplan, J., Dhariwal, P., et al. (2020). Language models are few-shot learners. *Advances in Neural Information Processing Systems*. <https://proceedings.neurips.cc/paper/2020/file/1457c0d6bfc4967418bfb8ac142f64a-Paper.pdf>

Choromanski, K., Likhoshesterov, V., Dohan, D., Song, X., Gane, A., Sarlos, T., Hawkins, P., Davis, J., Mohiuddin, A., Kaiser, L., Belanger, D., Colwell, L., & Weller, A. (2021). Rethinking attention with performers. *ICLR*. <https://arxiv.org/abs/2009.14794>

Clark, K., Luong, M.-T., Le, Q. V., & Manning, C. D. (2020). Electra: Pre-training text encoders as discriminators rather than generators. *ICLR*. <https://arxiv.org/abs/2003.10555>

Dai, Z., Yang, Z., Yang, Y., Carbonell, J., Le, Q., & Salakhutdinov, R. (2019). Transformer-xl: Attentive language models beyond a fixed-length context. *ACL*. <https://arxiv.org/abs/1901.02860>

Dettmers, T., Pagnoni, A., Holtzman, A., & Zettlemoyer, L. (2023). Qlora: Efficient finetuning of quantized llms. *Advances in Neural Information Processing Systems*. <https://arxiv.org/abs/2305.14314>

Devlin, J., Chang, M.-W., Lee, K., & Toutanova, K. (2019). Bert: Pre-training of deep bidirectional transformers for language understanding. *Proceedings of the 2019 Conference of the North American Chapter of the Association for Computational Linguistics: Human Language Technologies (NAACL-HLT)*. <https://aclanthology.org/N19-1423/>

Ding, N., et al. (2023). Parameter-efficient fine-tuning of large-scale pre-trained language models: A survey. *arXiv preprint arXiv:2303.15647*. <https://arxiv.org/abs/2303.15647>

Gage, P. (1994). A new algorithm for data compression. *C Users Journal*, 12(2).

Goldberger, A. L., Amaral, L. A. N., Glass, L., Hausdorff, J. M., Ivanov, P. C., Mark, R. G., Mietus, J. E., Moody, G. B., Peng, C.-K., & Stanley, H. E. (2000). Physiobank, physiotoolkit, and physionet: Components of a new research resource for complex physiologic signals [RRID:SCR_007345]. *Circulation*, 101(23), e215–e220. <https://physionet.org/about/publications/>

Goodfellow, I., Bengio, Y., & Courville, A. (2016). *Deep learning*. MIT Press. <https://www.deeplearningbook.org/>

Gu, Y., Tinn, R., Cheng, H., Lucas, M., Usuyama, N., Liu, X., Naumann, T., Gao, J., & Poon, H. (2021). Domain-specific language model pretraining for biomedical natural language processing. *ACL*. <https://arxiv.org/abs/2007.15779>

Gururangan, S., Marasovic, A., Swayamdipta, S., Lo, K., Beltagy, I., Downey, D., & Smith, N. A. (2020). Don't stop pretraining: Adapt language models to domains and tasks. *Proceedings of the 58th Annual Meeting of the Association for Computational Linguistics (ACL)*. <https://aclanthology.org/2020.acl-main.740/>

He, K., et al. (2016). Deep residual learning for image recognition. *Proceedings of the IEEE Conference on Computer Vision and Pattern Recognition*.

Hendrycks, D., & Gimpel, K. (2016). Gaussian error linear units (gelus). *arXiv preprint arXiv:1606.08415*.

Houlsby, N., Giurgiu, A., Jastrzebski, S., Morrone, B., de Laroussilhe, Q., Gesmundo, A., Attariyan, M., & Gelly, S. (2019). Parameter-efficient transfer learning for nlp. *Proceedings of the 36th International Conference on Machine Learning (ICML)*, 97, 2790–2799. <https://proceedings.mlr.press/v97/houlsby19a.html>

Howard, J., & Ruder, S. (2018). Universal language model fine-tuning for text classification. *ACL*. <https://arxiv.org/abs/1801.06146>

Hu, E. J., Shen, Y., Wallis, P., Allen-Zhu, Z., Li, Y., Wang, S., & Chen, W. (2022). Lora: Low-rank adaptation of large language models. *ICLR*. <https://arxiv.org/abs/2106.09685>

Huang, K., Altosaar, J., & Ranganath, R. (2019). Clinicalbert: Modeling clinical notes and predicting hospital readmission. *arXiv preprint arXiv:1904.05342*. <https://arxiv.org/abs/1904.05342>

Irvin, J., Rajpurkar, P., Ko, M., Yu, Y., Ciurea-Ilcus, S., Chute, C., Marklund, H., Haghgoo, B., Ball, R., Shpanskaya, K., Seekins, J., Mong, D. A., Halabi, S. S., Sandberg, J. K., Jones, R., Larson, D. B., Langlotz, C. P., Patel, B. N., Lungren, M. P., & Ng, A. Y. (2019). Chexpert: A large chest radiograph dataset with uncertainty labels and expert comparison. *arXiv preprint arXiv:1901.07031*. <https://arxiv.org/abs/1901.07031>

Irvin, J., Rajpurkar, P., Ko, M., Yu, Y., Ciurea-Ilinca, F., Chute, C., Marklund, H., Haghgoo, B., Ball, R., Shpanskaya, K., Seekins, J., Mong, D. A., Halabi, S. S., Sandberg, J. K., Jones, R., Larson, D. B., Langlotz, C. P., Patel, B. N., Lungren, M. P., & Ng, A. Y. (2019). Chexpert: A large chest radiograph dataset with uncertainty labels and expert comparison. *arXiv preprint arXiv:1901.07031*. <https://arxiv.org/abs/1901.07031>

Jiang, Z., et al. (2023). A survey of large language models for healthcare. *arXiv preprint arXiv:2303.01246*. <https://arxiv.org/abs/2303.01246>

Johnson, A. E. W., Bulgarelli, L., Pollard, T. J., Horng, S., Celi, L. A., & Mark, R. G. (2023). Mimic-iv, a freely accessible electronic health record dataset. *Scientific Data*, 10(1), 1–10. <https://www.nature.com/articles/s41597-022-01899-x>

Johnson, A. E. W., Pollard, T. J., Berkowitz, S., Greenbaum, N. R., Lungren, M. P., Deng, C., Mark, R. G., & Horng, S. (2019). Mimic-cxr: A large publicly available database of labeled chest radiographs. *arXiv preprint arXiv:1901.07042*. <https://physionet.org/content/mimic-cxr/2.0.0/>

Johnson, A. E. W., Pollard, T. J., Shen, L., Li-Wei, H. L., Feng, M., Ghassemi, M., Moody, B., Szolovits, P., Celi, L. A., & Mark, R. G. (2016). Mimic-iii, a freely accessible critical care database. *Scientific Data*. <https://www.nature.com/articles/sdata201635>

Kitaev, N., Kaiser, L., & Levskaya, A. (2020). Reformer: The efficient transformer. *ICLR*. <https://arxiv.org/abs/2001.04451>

Lan, Z., Chen, M., Goodman, S., Gimpel, K., Sharma, P., & Soricut, R. (2020). Albert: A lite bert for self-supervised learning of language representations. *ICLR*. <https://arxiv.org/abs/1909.11942>

Lee, J., Yoon, W., Kim, S., Kim, D., Kim, S., So, C., & Kang, J. (2020). Biobert: A pre-trained biomedical language representation model for biomedical text mining. *Bioinformatics*. <https://academic.oup.com/bioinformatics/article/36/4/1234/5566506>

Lester, B., Al-Rfou, R., & Constant, N. (2021). The power of scale for parameter-efficient prompt tuning. *EMNLP*. <https://arxiv.org/abs/2104.08691>

Li, F., & Yu, H. (2019). Caml: Convolutional attention-based multi-label learning for icd coding. *AAAI*. <https://ojs.aaai.org/index.php/AAAI/article/view/3806>

Li, X. L., & Liang, P. (2021). Prefix-tuning: Optimizing continuous prompts for generation. *Proceedings of the 59th Annual Meeting of the Association for Computational Linguistics (ACL)*. <https://aclanthology.org/2021.acl-long.353/>

Liu, H., Tam, D., Muqeeth, M., Mohta, J., Huang, T., Bansal, M., & Raffel, C. (2022). Few-shot parameter-efficient fine-tuning is better and cheaper than in-context learning. *NeurIPS*. <https://arxiv.org/abs/2205.05638>

Liu, X., Zheng, Y., Du, Z., Ding, M., Qian, Y., Yang, Z., & Tang, J. (2021). P-tuning: Prompt tuning can be comparable to fine-tuning across scales and tasks. *arXiv preprint arXiv:2103.10385*. <https://arxiv.org/abs/2103.10385>

Liu, Y., Ott, M., Goyal, N., Du, J., Joshi, M., Chen, D., Levy, O., Lewis, M., Zettlemoyer, L., & Stoyanov, V. (2019). Roberta: A robustly optimized bert pretraining approach. *arXiv preprint arXiv:1907.11692*. <https://arxiv.org/abs/1907.11692>

Loshchilov, I., & Hutter, F. (2019). Decoupled weight decay regularization. *ICLR*. <https://arxiv.org/abs/1711.05101>

Mullenbach, J., Wiegreffe, S., Duke, J., Sun, J., & Eisenstein, J. (2018). Explainable prediction of medical codes from clinical text. *Proceedings of NAACL-HLT 2018*. <https://doi.org/10.18653/v1/N18-1100>

On layer normalization in the transformer architecture. (2020). *ICLR*. <https://arxiv.org/abs/2002.04745>

OpenAI. (2019). *Gpt-2: 1.5b release*. <https://openai.com/index/gpt-2-1-5b-release/>

Paszke, A., Gross, S., Massa, F., Lerer, A., Bradbury, J., Chanan, G., et al. (2019). Pytorch: An imperative style, high-performance deep learning library. *Advances in Neural Information Processing Systems*, 32.

Peters, M. E., Neumann, M., Iyyer, M., Gardner, M., Clark, C., Lee, K., & Zettlemoyer, L. (2018). Deep contextualized word representations. *NAACL*. <https://arxiv.org/abs/1802.05365>

Peters, M. E., Ruder, S., & Smith, N. A. (2019). To tune or not to tune? adapting pretrained representations to diverse tasks. *ACL Workshop*. <https://arxiv.org/abs/1903.05987>

Pfeiffer, J., et al. (2021). Adapterfusion: Non-destructive task composition for transfer learning. *EACL*. <https://arxiv.org/abs/2005.00247>

Press, O., & Wolf, L. (2017). Using the output embedding to improve language models. *EACL*. <https://arxiv.org/abs/1608.05859>

Radford, A., Narasimhan, K., Salimans, T., & Sutskever, I. (2018). Improving language understanding by generative pre-training. *OpenAI Technical Report*. https://cdn.openai.com/research-covers/language-unsupervised/language_understanding_paper.pdf

Radford, A., Wu, J., Child, R., Luan, D., Amodei, D., & Sutskever, I. (2019). Language models are unsupervised multitask learners. *OpenAI Technical Report*. <https://openai.com/research/language-models>

Raffel, C., Shazeer, N., Roberts, A., Lee, K., Narang, S., Matena, M., Zhou, Y., Li, W., & Liu, P. J. (2020). Exploring the limits of transfer learning with a unified text-to-text transformer. *JMLR*. <https://arxiv.org/abs/1910.10683>

Sennrich, R., Haddow, B., & Birch, A. (2016). Neural machine translation of rare words with subword units. *Proceedings of the 54th Annual Meeting of the Association for Computational Linguistics*.

Shin, H.-C., et al. (2020). Biomegatron: Larger biomedical domain language model. *arXiv preprint arXiv:2010.06060*. <https://arxiv.org/abs/2010.06060>

Singhal, K., et al. (2023). Large language models encode clinical knowledge. *Nature*. <https://www.nature.com/articles/s41586-023-06291-2>

Srivastava, N., Hinton, G., Krizhevsky, A., Sutskever, I., & Salakhutdinov, R. (2014). Dropout: A simple way to prevent neural networks from overfitting. *Journal of Machine Learning Research*, 15(1), 1929–1958. <https://jmlr.org/papers/v15/srivastava14a.html>

Uzuner, O., et al. (2011). Evaluating the state of the art in coreference resolution for electronic medical records. *Journal of the American Medical Informatics Association*. <https://academic.oup.com/jamia/article/19/5/786/683705>

Vaswani, A., Shazeer, N., Parmar, N., Uszkoreit, J., Jones, L., Gomez, A. N., Kaiser, L., & Polosukhin, I. (2017). Attention is all you need. *Advances in Neural Information Processing Systems*, 30. <https://papers.neurips.cc/paper/7181-attention-is-all-you-need.pdf>

Wang, S., Li, B. Z., Khabsa, M., Fang, H., & Ma, H. (2020). Linformer: Self-attention with linear complexity. *arXiv preprint arXiv:2006.04768*. <https://arxiv.org/abs/2006.04768>

Wolf, T., Debut, L., Sanh, V., Chaumond, J., Delangue, C., Moi, A., Cistac, P., Rault, T., Louf, R., Funtowicz, M., & Brew, J. (2020). Transformers: State-of-the-art natural language processing. *Proceedings of the 2020 Conference on Empirical Methods in Natural Language Processing: System Demonstrations*, 38–45. <https://aclanthology.org/2020.emnlp-demos.6/6>

Xu, J., et al. (2020). Understanding and improving transformer from a multi-particle dynamic system point of view. *arXiv preprint arXiv:2002.04745*.

Yang, Z., Dai, Z., Yang, Y., Carbonell, J., Salakhutdinov, R., & Le, Q. V. (2019). Xlnet: Generalized autoregressive pre-training for language understanding. *NeurIPS*. <https://arxiv.org/abs/1906.08237>

Yosinski, J., Clune, J., Bengio, Y., & Lipson, H. (2014a). How transferable are features in deep neural networks? *NeurIPS*. <https://arxiv.org/abs/1411.1792>

Yosinski, J., Clune, J., Bengio, Y., & Lipson, H. (2014b). How transferable are features in deep neural networks? *Advances in Neural Information Processing Systems*. <https://arxiv.org/abs/1411.1792>

Zaheer, M., Guruganesh, G., Dubey, A., Ainslie, J., Alberti, C., Ontanon, S., Pham, P., Ravula, A., Wang, Q., Yang, L., & Ahmed, A. (2020). Big bird: Transformers for longer sequences. *Advances in Neural Information Processing Systems*. https://papers.neurips.cc/paper_files/paper/2020/file/c8512d142a2d849725f31a9a7a361ab9-Paper.pdf

Zaken, E. B., Ravfogel, S., & Goldberg, Y. (2022). Bitfit: Simple parameter-efficient fine-tuning for transformer-based masked language-models. *ACL Findings*. <https://arxiv.org/abs/2106.10199>